



HAL
open science

Efficient synthesis, crystal structure, Hirshfeld surface analysis, biological evaluation, DFT calculations and Docking study of pyrano[4,3-b]pyran derivatives

Yasmine Zine, Mohamed Abdesselem Dems, Raouf Boulcina, Ali Boudjada, Dominique Harakat, Thierry Roisnel, Anthony Robert, Abdelmadjid Debache

► To cite this version:

Yasmine Zine, Mohamed Abdesselem Dems, Raouf Boulcina, Ali Boudjada, Dominique Harakat, et al.. Efficient synthesis, crystal structure, Hirshfeld surface analysis, biological evaluation, DFT calculations and Docking study of pyrano[4,3-b]pyran derivatives. *Journal of Molecular Structure*, 2024, 1300, pp.137256-137256. 10.1016/j.molstruc.2023.137256 . hal-04343933

HAL Id: hal-04343933

<https://hal.science/hal-04343933>

Submitted on 18 Apr 2024

HAL is a multi-disciplinary open access archive for the deposit and dissemination of scientific research documents, whether they are published or not. The documents may come from teaching and research institutions in France or abroad, or from public or private research centers.

L'archive ouverte pluridisciplinaire **HAL**, est destinée au dépôt et à la diffusion de documents scientifiques de niveau recherche, publiés ou non, émanant des établissements d'enseignement et de recherche français ou étrangers, des laboratoires publics ou privés.



Distributed under a Creative Commons Attribution - NonCommercial 4.0 International License

Highlights

- A highly efficient method for the synthesis of 4-Arylidene-1*H*-Pyrazol-5(4*H*)-one derivatives has been achieved using PPTS as a catalyst.
- The use of environmentally friendly solvents
- The synthesized 4-Arylidene-1*H*-pyrazol-5(4*H*)-ones were screened for their anti-Alzheimer and antimicrobial activities
- The compounds are obtained with good yields in short time of 30 minutes
- The implementation of the reaction is easy without column chromatography.

Efficient synthesis, crystal structure, Hirshfeld surface analysis, biological evaluation, DFT calculations and Docking study of pyrano[4,3-*b*]pyran derivatives

Yasmine Zine¹, Mohamed Abdesselem Dems², Raouf Boulcina¹, Ali Boudjada³, Dominique Harakat⁴, Thierry Roisnel⁵, Anthony Robert⁴, Abdelmadjid Debache^{1*}

¹Laboratoire de Synthèse de Molécules d'intérêts biologiques, Université Frères Mentouri Constantine 1, 25000 Constantine, Algeria.

²Unité Bioinformatique et biostatistique, Centre de Recherche en Biotechnologie (CRBT Constantine), Constantine, Algeria

³Laboratoire de Cristallographie, Université Frères Mentouri Constantine 1, 25000 Constantine, Algeria

⁴URCA Tech, ICMR, CNRS UMR 7312, URCA Bat. 18 B.P. 1039, 51687, Reims, Cedex 2, France.

⁵Université Rennes, CNRS, ISCR (Institut des Sciences Chimiques de Rennes), UMR 6226, F- 35000 Rennes, France. .

*Corresponding author: a_debache@yahoo.fr.

Abstract

In this work we describe a simple and rapid method for the synthesis of a series of pyrano[4,3-*b*]pyran derivatives by a three-component reaction between 4-hydroxy-6-methylpyran-2-one, malononitrile and a variety of aromatic and heteroaromatic aldehydes. The reactions are carried out at reflux of a water/ethanol mixture in the presence of 10 mol% of pyridinium *p*-toluenesulfonate as catalyst with excellent yields of expected products. The antimicrobial and anti-Alzheimer's activities of the prepared products were evaluated and some molecules gave interesting results. In addition, theoretical studies such as Density Functional Theory (DFT), IR and UV-visible spectra and molecular docking have also been carried out. Moreover, the molecular structure of one compound was confirmed by X-ray diffraction analysis with its Hirshfeld surface analysis.

Keywords

pyrano[4,3-*b*]pyran, three-component reaction, antimicrobial evaluation, Density Functional Theory, molecular docking.

1. Introduction

The first multicomponent reactions were described by Laurent-Gerhardt in 1838 [1] then by Strecker in 1850 [2]. Since then, several others have been reported and they have undergone considerable development and have become one of the most powerful tools for the synthesis of heterocycles of diverse structures. In recent years, a three-component reaction between 4-hydroxy-6-methylpyran-2-one, malononitrile and aromatic aldehydes has been described and carried out in the presence of several types of catalysts such as MgO [3], DBU [4], NH₄OAc [5], NaBr/electrolysis [6], H₆P₂W₁₈O₆₂ [7], several ionic liquids [8-11], nano CaO [12], thiourea dioxide [13], Also were successfully used succinimide-N-sulfonic acid [14], sodium ethylene diamine tetraacetate [15], lipase [16], Z(L-proline)₂ [17], MNPs@Cu [18], 4,4'-trimethylene dipeperidine [19], nano-cell-OBf₂ [20], piperazinediethanesulfonic acid [21], cysteic acid grafted graphene oxide [22], MNPs SrFe₁₂O₁₉ [23], Zn₂SnO₄-SnO₂ [24].

In recent years, computer calculations such as DFT, molecular docking which makes it possible to predict possible biological activities, the study of geometry and other molecular characteristics have become useful tools in organic chemistry [25,26].

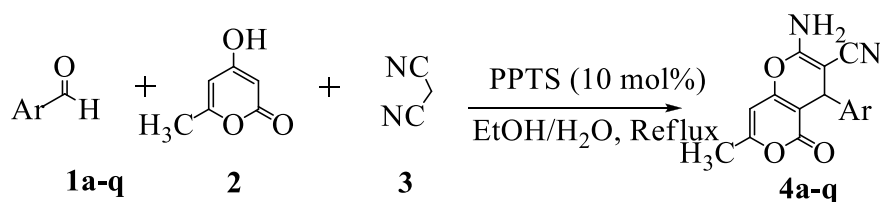
Alzheimer's disease, a degenerative disease, has become a serious public health problem and the search of possible treatment is a priority for many researchers [27].

The interest of 4-hydroxy-6-methylpyran-2-one derivatives lies in their broad spectrum of biological activities. They are described as anticonvulsant and antimicrobial [28], antiviral and antileishmanial [26], antitumor and antioxidant [5], antimycobacterial [9] and anticancer [30].

Continuing our search for new synthetic procedures of heterocyclic compounds [31-34], we report in the present work the catalytic effect of pyridinium *para*-toluenesulfonate (PPTS) on the three-component reaction between 4-hydroxy-6-methylpyran-2-one, malononitrile and aromatic aldehydes in a hydroalcoholic medium according to the scheme below (**Scheme 1**).

In addition, the work is completed by the evaluation of the anti-Alzheimer and antimicrobial activities of the synthesized compounds and by theoretical studies such as Density Functional Theory (DFT) calculations, IR and UV-visible vibration analysis and molecular docking [35-38]. Furthermore, the structure of compound **4p** was confirmed by X-ray analysis and its Hirshfeld surface analyzed.

Moreover, we have already used this catalyst successfully in the synthesis of 2-amino-4*H*-pyrans [39], 1,4-benzoxazine derivatives [40] and 4-arylmethylidene-isoxazol-5(4*H*)-ones [41]. .



Scheme 1. Synthesis of 2-amino-4-(aryl)-7-methyl-5-oxo-4*H*,5*H*-pyrano[4,3-*b*]pyran-3-carbonitriles catalyzed by PPTS

2. Experimental part

2.1. Materiel and methods

Solvents and reagents are obtained commercially and used without further purification. The ¹H and ¹³C NMR spectra were recorded on a Bruker Advance DPX device at 500 MHz and 125.8 MHz respectively, with the TMS as internal reference. The chemical shifts are expressed in parts per million (ppm) and the coupling constants (*J*) in Hz. The monitoring of the reaction was carried out by thin layer chromatography (TLC) and was carried out using plates of silica gel Kieselgel F254 (Merck). Melting points are measured using a Kofler apparatus and are uncorrected. Mass spectra were recorded on a Synapt-G2 HDMS Traveling Wave-Ion Mobility (TWIMS) instrument equipped with an electrospray source (Waters, Manchester, UK). A suitable crystal for X-ray diffraction was selected and mounted with a cryoloop on the goniometer head of a D8 Venture (Bruker-AXS) diffractometer equipped with a CMOS-PHOTON70 detector, using Mo-K α radiation ($\lambda = 0.71073 \text{ \AA}$, multilayer monochromator) at $T = 150(2) \text{ K}$.

2.2. Synthesis

2.2.1. General procedure for the synthesis of 2-amino-4-(aryl)-7-methyl-5-oxo-4*H*,5*H*-pyrano[4,3-*b*]pyran-3-carbonitriles (4a-p)

A mixture of aldehyde (1 mmol), malononitrile (1 mmol), 4-hydroxy-6-methylpyran-2-one (1 mmol) and 10 mol% of PPTS in 5 ml of EtOH/H₂O (1/1) is refluxed for the appropriate time.

The reaction is followed by TLC. After cooling, the solid formed is filtered, washed with cold water and recrystallized from Ethanol.

Spectral data for compounds 4a-p

2-amino-7-methyl-5-oxo-4-phenyl-4H, 5H-pyrano [4, 3-b] pyran-3-carbonitrile (4a)

^1H NMR (500 MHz, DMSO- d_6): δ 7.33-7.29 (m, 2H, arom), 7.24-7.17 (m, 3H, arom), 7.19 (s, 2H, NH₂), 6.27 (s, 1H, CH), 4.28 (s, 1H, CH), 2.22 (s, 3H, CH₃). ^{13}C NMR (125.8 MHz, DMSO- d_6) δ 162.91, 161.33, 158.16, 158.07, 143.60, 128.41, 127.48, 126.97, 119.30, 100.74, 97.92, 57.91, 36.28, 19.29; HRMS (ESI⁺): m/z [M + H]⁺ calculated for C₁₆H₁₃N₂O₃ 281.0926, found 281.0929

2-amino-4-(4-chlorophenyl)-7-methyl-5-oxo-4H, 5H-pyrano [4, 3-b] pyran-3-carbonitrile (4b)

^1H NMR (500 MHz, DMSO- d_6): δ 7.37 (d, J = 8.46, 2H, arom), 7.24-7.21 (m, 2H, arom, 2H, NH₂), 6.27 (s, 1H, CH), 4.31 (s, 1H, CH), 2.22 (s, 3H, CH₃). ^{13}C NMR (125.8 MHz, DMSO- d_6) δ 163.09, 161.29, 158.25, 158.05, 142.57, 131.53, 129.47, 128.35, 110.15, 100.23, 97.94, 57.41, 35.72, 19.29; HRMS (ESI⁺): m/z [M + Na]⁺ calculated for C₁₆H₁₁ClN₂O₃Na 337.0358, found 337.0359.

2-amino-7-methyl-4-(2-nitrophenyl)-5-oxo-4H, 5H-pyrano [4, 3-b] pyran-3-carbonitrile (4c)

^1H NMR (500 MHz, DMSO- d_6): δ 7.87-7.85 (m, 1H, arom), 7.68-7.65 (m, 1H, arom), 7.49-7.42 (m, 1H, arom), 7.36 (s, 2H, NH₂), 6.28 (s, 1H, CH), 5.07 (s, 1H, CH), 2.20 (s, 3H, CH₃). ^{13}C NMR (125.8 MHz, DMSO- d_6) δ 163.37, 161.43, 158.73, 158.28, 149.24, 137.52, 133.56, 130.95, 128.32, 123.87, 118.77, 100.06, 97.97, 55.95, 30.95, 19.30; HRMS (ESI⁺): m/z [M + H]⁺ calculated for C₁₆H₁₂N₃O₅ 326.0777, found 326.0779.

2-amino-7-methyl-4-(3-nitrophenyl)-5-oxo-4H, 5H-pyrano [4, 3-b] pyran-3-carbonitrile (4d)

^1H NMR (500 MHz, DMSO- d_6): δ 8.12-8.10 (m, 1H, arom), 8.05-8.04 (m, 1H, arom), 7.37-7.71 (m, 1H, arom), 7.64-7.62 (m, 1H, arom), 7.35 (s, 2H, NH₂), 6.31 (s, 1H, CH), 4.56 (s, 1H, CH), 2.22 (s, 3H, CH₃). ^{13}C NMR (125.8 MHz, DMSO- d_6) δ 163.46, 161.34, 158.56, 158.26, 147.78, 145.76, 134.59, 130.05, 122.18, 119.01, 99.65, 98.03, 56.82, 35.96, 19.33; HRMS (ESI⁺): m/z [M + H]⁺ calculated for C₁₆H₁₂N₃O₅ 326.0777, found 326.0783.

2-amino-7-methyl-4-(4-nitrophenyl)-5-oxo-4H, 5H-pyrano [4, 3-b] pyran-3-carbonitrile (4e)

^1H NMR (500 MHz, DMSO- d_6): δ 8.18 (d, J = 8.7, 2H, arom), 7.50 (d, J = 8.7, 2H, arom), 7.34 (s, 2H, NH₂), 6.31 (s, 1H, CH), 4.50 (s, 1H, CH), 2.23 (s, 3H, CH₃). ^{13}C NMR (125.8 MHz, DMSO- d_6) δ 163.48, 161.31, 158.61, 158.17, 151.01, 140.54, 129.03, 123.68, 118.96, 99.56, 98.01, 56.66, 36.14, 19.33; HRMS (ESI⁺): m/z [M + H]⁺ calculated for C₁₆H₁₂N₃O₅ 326.0777, found 326.0782.

2-amino-4-(2-methoxyphenyl)-7-methyl-5-oxo-4H, 5H-pyrano [4, 3-b] pyran-3-carbonitrile (4f)

^1H NMR (500 MHz, DMSO- d_6): δ 7.22-7.18 (m, 1H, arom), 7.03-7.01 (m, 1H, arom, 2H, NH₂), 6.98-6.96 (m, 1H, arom), 6.88-6.85 (m, 1H, arom), 6.25 (s, 1H, CH), 4.51 (s, 1H, CH), 3.72 (s, 3H, CH₃), 2.21 (s, 3H, CH₃). ^{13}C NMR (125.8 MHz, DMSO- d_6) δ 162.53, 161.33, 158.82, 158.64, 157.15, 130.98, 129.04, 128.30, 120.43, 119.46, 111.74, 100.02, 97.86, 56.86, 55.69, 31.61, 19.29; HRMS (ESI⁺): m/z [M + Na]⁺ calculated for C₁₇H₁₄N₂O₄Na 333.0851, found 333.0855.

2-amino-4-(4-methoxyphenyl)-7-methyl-5-oxo-4H, 5H-pyrano [4, 3-b] pyran-3-carbonitrile (4g)

^1H NMR (500 MHz, DMSO- d_6): δ 7.14 (s, 2H, NH₂), 7.09 (d, J = 8.65, 2H, arom), 6.85 (d, J = 8.66, 2H, arom), 6.25 (s, 1H, CH), 4.21 (s, 1H, CH), 3.72 (s, 3H, CH₃), 2.21 (s, 3H, CH₃). ^{13}C NMR (125.8 MHz, DMSO- d_6) δ 162.72, 161.32, 158.22, 157.99, 157.86, 135.67, 128.58, 119.37, 113.75, 101.02, 97.91, 58.14, 55.04, 35.48, 19.27; HRMS (ESI⁺): m/z [M + Na]⁺ calculated for C₁₇H₁₄N₂O₄Na 333.0851, found 333.0858.

2-amino-7-methyl-5-oxo-4-(o-tolyl)-4H, 5H-pyrano [4, 3-b] pyran-3-carbonitrile (4h)

^1H NMR (500 MHz, DMSO- d_6): δ 7.20-7.17 (m, 1H, arom, 2H, NH₂), 7.04-7.03 (m, 1H, arom), 6.97-6.96 (m, 2H, arom), 6.27 (s, 1H, CH), 4.22 (s, 1H, CH), 2.27 (s, 3H, CH₃), 2.22 (s, 3H, CH₃). ^{13}C NMR (125.8 MHz, DMSO- d_6) δ 162.84, 161.32, 158.13, 158.04, 143.58, 137.49, 128.29, 127.90, 127.69, 124.69, 119.32, 100.78, 97.94; HRMS (ESI⁺): m/z [M + H]⁺ calculated for C₁₇H₁₅N₂O₃ 295.1083, found 295.1082.

2-amino-7-methyl-5-oxo-4-(m-tolyl)-4H, 5H-pyrano [4, 3-b] pyran-3-carbonitrile (4i)

^1H NMR (500 MHz, DMSO- d_6): δ 7.20-7.17 (m, 1H, arom, 2H, NH₂), 7.04-7.03 (m, 1H, arom), 6.97-6.96 (m, 2H, arom), 6.26 (s, 1H, CH), 4.23 (s, 1H, CH), 2.27 (s, 3H, CH₃), 2.21 (s, 3H, CH₃). ^{13}C NMR (125.8 MHz, DMSO- d_6) δ 162.84, 161.33, 158.13, 158.05, 143.59,

137.48, 128.30, 127.91, 127.70, 124.70, 119.33, 100.79, 97.94, 58.02, 36.23, 21.05, 19.29; HRMS (ESI⁺): m/z [M + H]⁺ calculated for C₁₇H₁₅N₂O₃ 295.1083, found 295.1086.

2-amino-7-methyl-5-oxo-4-(p-tolyl)-4H, 5H-pyrano [4, 3-b] pyran-3-carbonitrile (4j)

¹H NMR (500 MHz, DMSO-*d*₆): δ 7.15 (s, 2H, NH₂), 7.11-7.09 (m, 2H, arom), 7.07-7.05 (m, 2H, arom), 6.25 (s, 1H, CH), 4.22 (s, 1H, CH), 2.25 (s, 3H, CH₃), 2.21 (s, 3H, CH₃). ¹³C NMR (125.8 MHz, DMSO-*d*₆) δ 162.79, 161.31, 158.02, 140.66, 136.10, 128.95, 127.38, 119.33, 100.88, 97.91, 58.04, 35.89, 20.61, 19.28; HRMS (ESI⁺): m/z [M + H]⁺ calculated for C₁₇H₁₅N₂O₃ 295.1083, found 295.1085.

2-amino-7-methyl-5-oxo-4-(thiophen-2-yl)-4H, 5H-pyrano [4, 3-b] pyran-3-carbonitrile (4k)

¹H NMR (500 MHz, DMSO-*d*₆): δ 7.36 (dd, *J* = 3.7, 1H, arom), 7.31 (s, 2H, NH₂), 6.97-6.92 (m, 2H, arom), 6.26 (s, 1H, CH), 4.64 (s, 1H, CH), 2.22 (s, 3H, CH₃). ¹³C NMR (125.8 MHz, DMSO-*d*₆) δ 163.19, 161.26, 158.42, 157.82, 147.99, 126.92, 124.93, 124.88, 119.17, 100.79, 97.92, 57.76, 31.26, 19.32; HRMS (ESI⁺): m/z [M + H]⁺ calculated for C₁₄H₁₁N₂O₃S 287.0490, found 287.0491.

2-amino-4-(4-hydroxyphenyl)-7-methyl-5-oxo-4H, 5H-pyrano [4, 3-b] pyran-3-carbonitrile (4l)

¹H NMR (500 MHz, DMSO-*d*₆): δ 9.31 (s, 1H, OH), 7.10 (s, 2H, NH₂), 6.96 (d, *J*=8.5, 2H, arom), 6.67 (d, *J* = 8.51, 2H, arom), 6.24 (s, 1H, CH), 4.15 (s, 1H, CH), 2.20 (s, 3H, CH₃). ¹³C NMR (125.8 MHz, DMSO-*d*₆) δ 162.59, 161.34, 157.98, 157.77, 156.35, 133.99, 128.51, 119.45, 115.07, 101.24, 97.92, 58.35, 35.47, 19.27; HRMS (ESI⁺): m/z [M + H]⁺ calculated for C₁₆H₁₃N₂O₄ 297.0875, found 297.0874.

2-amino-4-(1H-imidazol-5-yl)-7-methyl-5-oxo-4H, 5H-pyrano [4, 3-b] pyran-3-carbonitrile (4m)

¹H NMR (500 MHz, DMSO-*d*₆): δ 7.52 (s, 1H, imid), 7.03 (s, 2H, NH₂), 6.91 (s, 1H, imid), 6.21 (s, 1H, CH), 4.28 (s, 1H, CH), 2.20 (s, 3H, CH₃). ¹³C NMR (125.8 MHz, DMSO-*d*₆) δ 162.34, 161.46, 158.49, 158.22, 139.81, 134.93, 119.67, 114.51, 100.31, 98.05, 57.40, 29.27, 19.27; HRMS (ESI⁺): m/z [M + H]⁺ calculated for C₁₃H₁₁N₄O₃ 271.0831, found 271.0828.

(5-(2-amino-3-cyano-7-methyl-5-oxo-4H, 5H-pyrano [4, 3-b] pyran-4-yl) furan-2-yl) boronic acid (4n)

^1H NMR (500 MHz, DMSO- d_6): δ 8.06 (s, 2H, NH₂), 7.23 (s, 2H, OH), 6.96 (d, J = 3.21, 1H, fur), 6.27 (s, 1H, CH), 6.18 (d, J = 3.22, 1H, fur), 4.46 (s, 1H, CH), 2.23 (s, 3H, CH₃). ^{13}C NMR (125.8 MHz, DMSO- d_6) δ 163.02, 161.20, 158.69, 158.56, 158.29, 122.67, 119.08, 107.16, 98.15, 98.08, 55.34, 30.24, 19.32; HRMS (ESI⁺): m/z [M + H]⁺ calculated for C₁₄H₁₂N₂O₆B 315.0788, found 315.0793.

(4-(2-amino-3-cyano-7-methyl-5-oxo-4H, 5H-pyrano [4, 3-b] pyran-4-yl) phenyl) boronic acid (4o)

^1H NMR (500 MHz, DMSO- d_6): δ 7.99 (s, 2H, NH₂), 7.70 (d, J = 8.00, 2H, arom), 7.18 (s, 2H, OH), 7.13 (d, J = 8.08, 2H, arom), 6.27 (s, 1H, CH), 4.26 (s, 1H, CH), 2.22 (s, 3H, CH₃). ^{13}C NMR (125.8 MHz, DMSO- d_6) δ 162.91, 161.33, 158.20, 158.04, 145.33, 134.22, 126.56, 119.30, 100.63, 97.94, 57.83, 36.31, 19.31; HRMS (ESI⁺): m/z [M + H]⁺ calculated for C₁₆H₁₄N₂O₅B 325.0996, found 325.1000.

2-amino-4-(4-ethylphenyl)-7-methyl-5-oxo-4H, 5H-pyrano [4, 3-b] pyran-3-carbonitrile (4p)

^1H NMR (500 MHz, DMSO- d_6): δ 7.22-7.20 (m, 2H, arom), 7.17-7.15 (m, 2H, arom), 5.92 (s, 1H, CH), 4.68 (s, 2H, NH₂), 4.47 (s, 1H, CH), 2.63 (q, 2H, CH₂), 2.25 (s, 3H, CH₃), 1.22 (t, 3H, CH₃); ^{13}C NMR (125.8 MHz, DMSO- d_6) δ 162.49, 161.85, 157.62, 157.16, 143.52, 139.13, 128.20, 127.68, 118.25, 102.19, 97.86, 63.31, 35.86, 28.47, 20.00, 15.38; HRMS (ESI⁺): m/z [M + Na]⁺ calculated for C₁₈H₁₆N₂O₃Na 331.1059, found 331.1061.

2.3. Method for cholinesterase activity assay

Acetylcholinesterase (AChE) and butyrylcholinesterase (BChE) inhibitory activity was measured, by the spectrophotometric method developed by Ellman, G.L. *et al.* [42]. Briefly, 150 μl of 100 mM sodium phosphate buffer (pH 8.0), 10 μl of sample solution dissolved in methanol at different concentrations and 20 μl AChE (5.32×10^{-3} U) or BChE (6.85×10^{-3} U) solution were mixed and incubated for 15 min at 25 °C, and 10 μl of 0.5 mM DTNB[5,5'-dithio-bis(2-nitrobenzoic) acid] were added. The reaction was then initiated by the addition of 10 μl of acetylthiocholine iodide (0.71 mM) or butyrylthiocholine chloride (0.2 mM). The hydrolysis of these substrates were monitored spectrophotometrically by the formation of yellow 5-thio-2-nitrobenzoate anion, as the result of the reaction of DTNB with thiocholine, released by the enzymatic hydrolysis of acetylthiocholine iodide or

butyrylthiocholine chloride respectively at a wave length of 412 nm, every 5 min for 15 min, utilizing a 96-well microplate reader (PerkinElmer Multi-mode Plate Reader EnSpire, USA) in triplicate experiments. Galanthamine was used as reference compound. The results were given as 50% inhibition concentration (IC₅₀) and the percentage of inhibition of AChE or BChE was determined by comparison of re-action rates of samples relative to blank sample (methanol in phosphate buffer, pH 8) using the formula:

$$\text{Inhibition of AChE or BChE (\%)} = \frac{E - S}{E} \times 100$$

Where E is the activity of enzyme without test sample, and S is the activity of enzyme with test sample.

2.4. *In vitro* Antibacterial evaluation

2.4.1. Preparation of microorganism tests

The antibacterial activity of the tested compounds was evaluated using agar well diffusion and macrodilution method against six bacteria strains namely: *Bacillus cereus* (ATCC 10879), *Echerichia coli* (ATCC 25922), *Staphylococcus aureus* (ATCC 43300), *Klebsiella pneumonia* (ATCC 700603), *Pseudomonas aeruginosa* (ATCC 27853) and *Salmonella typhi* (ATCC 14028). The choice of bacterial strains was due to their clinical and pharmacological importance. Antibacterial tests were performed from young cultures (18 to 24h), in the exponential growth phase. The opacity of the bacterial suspensions in physiological sterile water was equivalent to 0.5 McFarland (a bacterial concentration estimated at 10⁶ CFU/ml) [43].

2.4.2. Agar well diffusion method

In this well-known procedure, agar plates on the Petri dishes are inoculated with a standardized inoculum of the test microorganism by the use of sterilized cotton swabs. After inoculation, wells were bored into the solidified agar surfaces on the Petri dishes by the use of 6 mm sterile cork borer and 10 mg/mL solution of each test compound in DMSO were introduced to the well. Before incubation at 37° C, the dishes were left for 2h at 4° C to allow the diffusion of the bioactive substances [44,45].

Results reading was done after 18 to 24h. The antibacterial activity was evaluated by measuring the zone of growth inhibition of bacteria surrounding the wells. Gentamicine, chloramphenicol, fosfomycine, amoxicilline+ acide and imipenem served as the positive

control. DMSO was taken as the negative control which did not produce any significant zone of inhibition. Any extending of inhibition zone around the wells, even a small diameter, was considered as a positive result. It should be noted that three repetitions were performed, and the diameters of the inhibition zones were measured in millimetre.

2.4.3. *Macrodilution method*

The minimum inhibitory concentration (MIC) for tested compounds was calculated using well-established macrodilution method [46]. The minimum concentration of an antibacterial agent that can avert the bacterial growth after overnight incubation is known as MIC. Initially, seven test tubes were freshly autoclaved followed by the addition of 1 mL sterile nutrient broth (NB) medium in each test tube. Next, 1 mL of tested compound was added in first test tube and mixed well to ensure the bubble free solution. In order to execute the process of serial dilution, 1 mL of obtained solution was then transferred into second test tube and continued up to seventh test tube. Further, the 10 μL of 1.5×10^8 CFU mL^{-1} (colony forming unit) diluted inoculums of bacterial suspension adjusted with McFarland 0.5 standard was added in all test tubes and incubated at 37°C for 24 hours after proper mixing. Further, for control samples three different test tubes were autoclaved and named as M (medium), M+I (medium +inoculums) and M+AC (medium + antibacterial compound) as shown in Scheme S1. For the negative control, 1 mL sterile NB media and 10 μL of 1.5×10^8 CFU mL^{-1} diluted inoculum of bacterial suspension were added into control test tube (M+I) to observe the growth of bacteria in the presence of medium. Similarly, for the positive control, 1 mL diluted antibacterial compound and sterile NB media were added into test tube (M+AC) to check the transparency of solution. Further, 1 mL sterile NB medium was poured in the blank control test tube (M) to check the sterility of medium and equipment. All these control test tubes were incubated at 37°C for 24 hours.

2.5. *Theoretical investigations*

2.5.1. *Materials and Methods*

We utilized computational methods to investigate the electronic structural properties and behavior of our molecules. Specifically, we employed Density Functional Theory (DFT) calculations using the Hybrid functionals: B3LYP (Becke-3-Lee-Yang-Parr) [47-50]. The molecular geometry was optimized using the Amsterdam Density function (ADF) software [51]. All theoretical calculations were performed in the gas phase without imposing any symmetry constraints.

2.5.2. Molecular docking and ADME-Toxicity studies

The molecules, after being optimized, were subjected to docking simulations within the active sites of proteins using the established AutoDockTools-1.5.6 (version: 1.5.6) with a standardized protocol. Specifically, compound **4c** underwent docking within the active sites of two bacterial protein receptors, namely *Bacillus cereus* and *Staphylococcus aureus*, with respective Protein Data Bank (PDB) codes (1gym and 5BS3) [50,51], sourced from Research Collaboratory for Structural Bioinformatics (RCSB) Protein Data Center (<http://www.rcsb.org>). The crystal structure of the two bacterial proteins was obtained from the Research Collaboratory for Structural Bioinformatics (RCS Protein Data Bank (<http://www.rcsb.org>). Initially, the molecular structure was constructed and subjected to energy minimization using the same function mentioned in the Materials and Methods section. The proteins underwent treatment involving water removal, addition of hydrogen, and repair of end residues, followed by the creation of an active pocket. Ultimately, the outcomes were visualized using Discovery Studio Visualizer [52-54], focusing on the conformations that exhibited the lowest free binding energies.

The docking protocol was validated by assessing the degree of variation using the Root Mean Square Deviation (RMSD).

The predicted ADME properties of the recently synthesized compounds **4a-p**, were evaluated using the ADMETlab 2.0 (Website: <https://admetmesh.scbdd.com/>) is an enhanced and improved version of the ADMETlab server, developed to predict the pharmacokinetics and toxicity of chemical compounds [55].

2.6. X-ray crystallographic studies

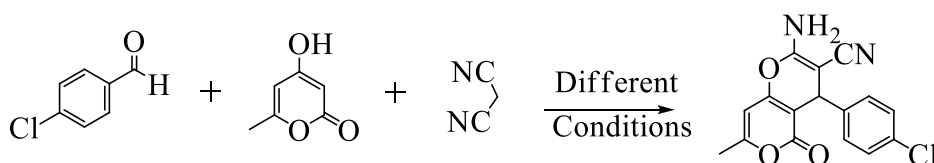
The crystal structure of the compound **4p** was analysed using a D8 Venture (Bruker-AXS) diffractometer equipped with a CMOS-PHOTON70 detector. The experiment used Mo-K α radiation ($\lambda = 0.71073 \text{ \AA}$, multilayer monochromator) at $T = 150(2) \text{ K}$. The data collection strategy for the crystal structure analysis was executed using the BIS V6.2.15/2021-03-15 and APEX4 2022.10-0 software. The crystal structure was solved by a dual-space algorithm using the SHELXT program [56] and then refined with full-matrix least-squares methods based on F^2 (SHELXL program) [57] All non-hydrogen atoms were refined with anisotropic atomic displacement parameters. Hydrogen atoms linked to nitrogen atoms were introduced in the

structural model through Fourier difference maps analysis. In contrast, other H atoms were included in their calculated positions and treated as riding on their parent atom with constrained thermal parameters. The crystallographic specifics for the compound **4p** are outlined in **Table 11**. The visual representations were generated utilising the Mercury software [58] The supplementary crystallographic data for this paper is catalogued under the CCDC number 2298326. This information is freely accessible from The Cambridge Crystallographic Data Centre through their website http://www.ccdc.cam.ac.uk/data_request/cif.

3. Results and discussion

3.1. Chemistry

To determine the optimal reaction conditions, we chose as a model an equimolar mixture of 4-chlorobenzaldehyde, malononitrile, 4-hydroxy-6-methylpyran-2-one and 10 mol% of PPTS which is subjected to different conditions (**Scheme 2**):



Scheme 2. Determination of optimal conditions.

In a first step, we determined the effect of the solvent and the temperature by working, for the sake of respecting nature, without solvent at 80°C, in H₂O, EtOH and H₂O/EtOH (1/1) at room temperature and reflux. A yield of 91% of pure product is obtained in H₂O/EtOH at reflux. This result being very satisfactory, we didn't test organic solvents.

In a second step, we examined the effect of catalytic quantity by varying it from 0% to 50% and 10 mol% leads to the best result in only 15 minutes. Therefore the optimal conditions for the reaction between 4-chlorobenzaldehyde, malonitrile and 4-hydroxy-6-methylpyran-2-one are 10 mol% of PPTS at reflux of H₂O/EtOH (1/1). The results are summarized in **Table 1**:

Table 1

Reaction optimization: effect of temperature, solvent and amount of catalyst

| Entry | Solvent | Catalyst (mol %) | Time (h) | Temperature (°C) | Yield (%) |
|-------|------------------------|------------------|----------|------------------|-----------|
| 1 | - | 10 | 24 | 80°C | Trace |
| 2 | H ₂ O | 10 | 10 | Ambiante | 30 |
| 3 | H ₂ O | 10 | 1 | Reflux | 67 |
| 4 | EtOH | 10 | 2.5 | Reflux | 62 |
| 5 | EtOH/ H ₂ O | 10 | 0.25 | Reflux | 91 |
| 6 | H ₂ O | - | 24 | Room temperature | Trace |
| 7 | H ₂ O | - | 5 | Reflux | 40 |
| 8 | EtOH/H ₂ O | - | 5 | Reflux | 45 |
| 9 | EtOH/H ₂ O | 5 | 0.25 | Reflux | 72 |
| 10 | EtOH/H ₂ O | 10 | 0.25 | Reflux | 91 |
| 11 | EtOH/H ₂ O | 20 | 0.25 | Reflux | 85 |
| 12 | EtOH/H ₂ O | 30 | 0.25 | Reflux | 79 |
| 13 | EtOH/H ₂ O | 50 | 0.25 | Reflux | 75 |

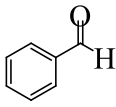
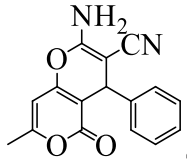
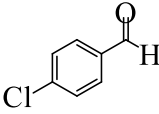
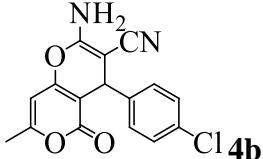
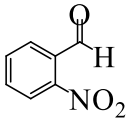
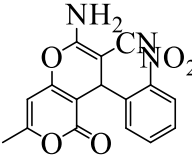
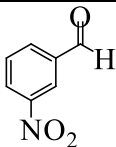
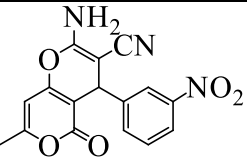
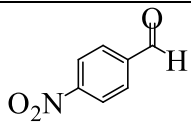
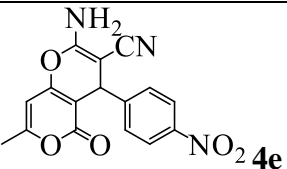
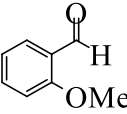
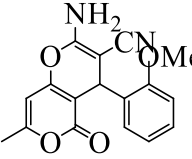
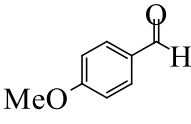
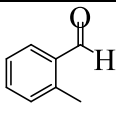
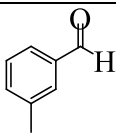
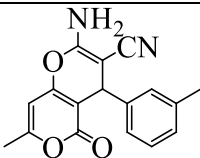
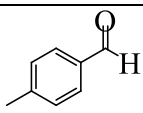
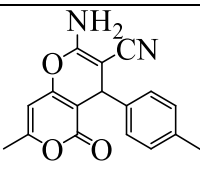
4-chlorobenzaldehyde/malonitrile/ 4-hydroxy-6-methyl-2*H*-pyran-2-one/PPTS: 1/1/1/0.1

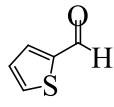
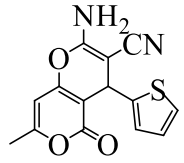
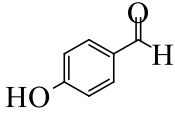
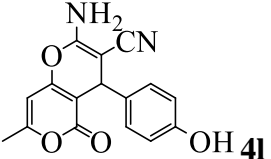
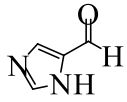
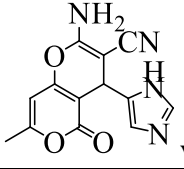
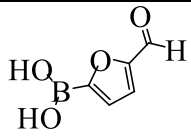
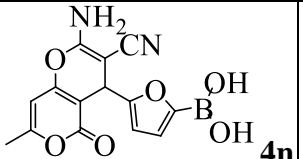
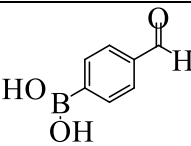
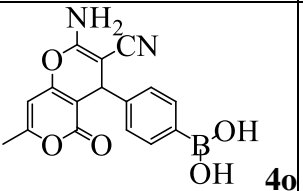
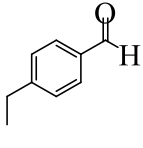
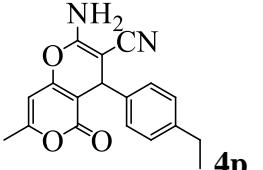
The optimal conditions were then applied to a long series of differently substituted aromatic and heteroaromatic aldehydes. The results are summarized in **Table 2**:

Table 2

2-Amino-4-(aryl)-7-methyl-5-oxo-4*H*,5*H*-pyrano[4,3-*b*]pyran-3-carbonitrile derivatives synthesis.

| Entry | Aldehydes | Product | Time (h) | Yield (%) | M.P | | |
|-------|-----------|---------|----------|-----------|-------|----------|-----|
| | | | | | Found | Reported | Ref |

| | | | | | | | |
|----|---|---|------|----|---------|---------|-------|
| 1 |  |  4a | 0.25 | 93 | 238-240 | 236-238 | [7] |
| 2 |  |  4b | 0.25 | 91 | 232-234 | 230-231 | [7] |
| 3 |  |  4c | 0.25 | 93 | >260 | 261-263 | [11] |
| 4 |  |  4d | 0.25 | 90 | 238-240 | 235-237 | [14] |
| 5 |  |  4e | 0.25 | 85 | 208-210 | 208-210 | [17] |
| 6 |  |  4f | 0.25 | 94 | 248-250 | 243-245 | [11] |
| 7 |  |  4g | 0.25 | 89 | 200-202 | 200-202 | [20] |
| 8 |  |  4h | 0.25 | 94 | >260 | X | [16]* |
| 9 |  |  4i | 0.25 | 95 | >260 | 250-252 | [15] |
| 10 |  |  4j | 0.25 | 92 | 225-227 | 224-225 | [7] |

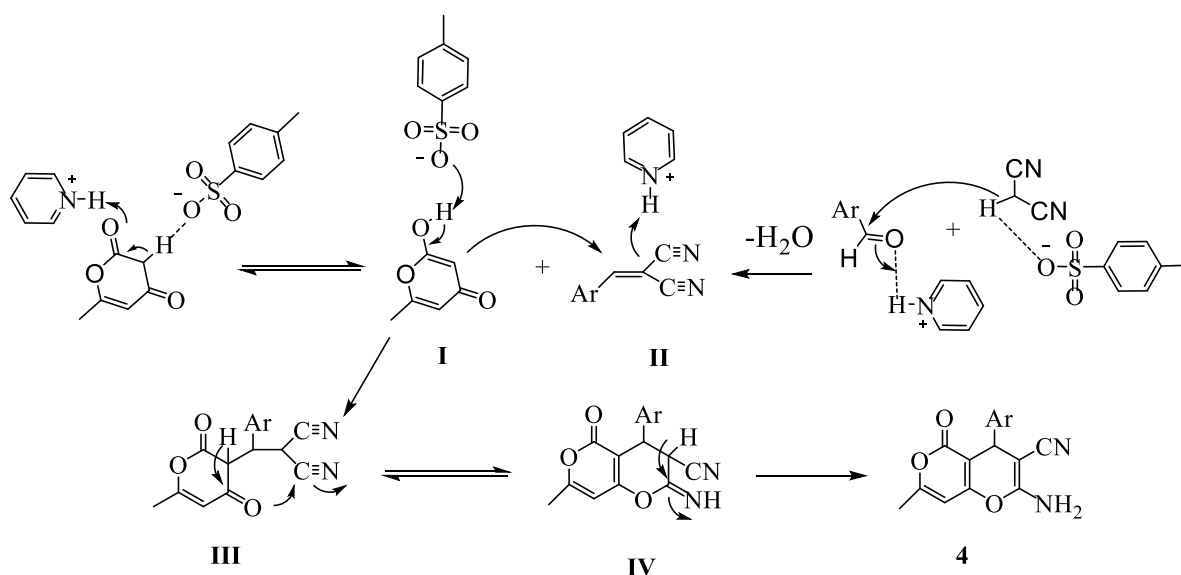
| | | | | | | | |
|----|---|--|------|----|---------|---------|------|
| 11 |  |  4k | 0.25 | 94 | 244-246 | 242-244 | [7] |
| 12 |  |  4l | 0.25 | 90 | >260 | 256-258 | [15] |
| 13 |  |  4m | 0.5 | 89 | 182-184 | - | - |
| 14 |  |  4n | 0.25 | 76 | >260 | - | - |
| 15 |  |  4o | 0.25 | 82 | >260 | - | - |
| 16 |  |  4p | 0.25 | 89 | | - | - |

aldehyde/malonitrile/4-hydroxy-6-methyl-2H-pyran-2-one/PPTS: 1/1/1/0.1

*Yield of pure product.

Table 2 shows that the expected products are obtained with excellent yields which vary between 76% and 95% (Entries 1 to 16) whatever the nature of the aldehyde, with very short reaction times between 0.25 and 0.5 hour.

We propose in the scheme below (**Scheme 4**) a possible mechanism of the formation of 2-amino-4-(aryl)-7-methyl-5-oxo-4*H*,5*H*-pyrano[4,3-*b*]pyran-3-carbonitriles by the three-component reaction between an aromatic aldehyde, 4-hydroxy-6-methylpyran-2-one and malononitrile catalyzed by PPTS. It appears that the catalyst intervenes in the formation of all the intermediates by acting on all the reactants.



Scheme 4. Mechanism of formation of 2-amino-4-(aryl)-7-methyl-5-oxo-4*H*,5*H*-pyrano[4,3-*b*]pyran-3-carbonitriles catalyzed by PPTS.

The 2-amino-4-(aryl)-7-methyl-5-oxo-4*H*,5*H*-pyrano[4,3-*b*]pyran-3-carbonitriles synthesis procedure catalyzed by PPTS proposed in this work was compared to those previously reported in the literature. As shown in **Table 3**, this comparison shows that our current method is among the most efficient with shorter reaction times, higher yields and lower amounts of catalyst. It is also compatible with the best in terms of respect for the environment.

Table 3

Comparison of the results of the synthesis of **4g** catalyzed by DMAP with those obtained with other catalysts.

| Entrée | catalyseur | Conditions | t (min) | Rdt (%) | Réf |
|--------|---|-----------------------------|---------|---------|------|
| 1 | BBSI-HSO ₄ (5 mol %) | Ball milling, r.t. | 30 | 90 | [11] |
| 2 | [DABCO : AcOH : H ₂ O] (1 :1 :3) | H ₂ O, r.t | 30 | 80 | [9] |
| 3 | TMDP (20 mol %) | Solvent-free, milling, r.t. | 30 | 84 | [10] |
| 4 | TMDPS (5 mol %) | Ball mill (600 rpm), r.t. | 30 | 90 | [11] |
| 5 | nano CaO | Solvent-free, 120°C | 300 | 94 | [12] |

| | | | | | |
|----|------------------------------------|-------------------------------|-----|----|-----------|
| 6 | PIPES (10 mol %) | Ball mill (600 rpm), r.t. | 30 | 86 | [21] |
| 7 | MgO (0.25g) | EtOH/H ₂ O, reflux | 37 | 85 | [3] |
| 8 | DBU (10mol %) | H ₂ O, reflux | 15 | 86 | [4] |
| 9 | SrFe ₁₂ O ₁₉ | Solvent-free, 120°C | 65 | 89 | [23] |
| 10 | Lipase | <i>i</i> -Propanol, 60° C | 600 | 85 | [16] |
| 11 | DBU | H ₂ O, Reflux | 15 | 86 | [4] |
| 12 | PPTS (10 mol %) | EtOH/H ₂ O, reflux | 15 | 89 | This work |

BBSI-HSO₄ : 1,1'-butylenebis (3-sulfo-3*H*-imidazol-1-ium) hydrogensulfate; **TMDP** : 4,4'-Trimethylenedipiperidine ; **TMDPS** : 4,4'-trimethylene-N,N'-sulfonic acid-dipiperidinium chloride ; **PIPES** : 1,4-Piperazinediethanesulfonic acid ; **Fe₃O₄@SiO₂/DABCO**: magnetic double-charged diazoniabicyclo[2.2.2]octane dichloride silica hybrid .

3.2. Biology evaluation

3.2.1. Evaluation of AChE and BChE inhibition

Acetylcholinesterase (AChE) and butyrylcholinesterase (BChE) inhibitory activities of selected compounds have been measured by the spectrophotometric method developed by Ellman et al. [42]. The inhibition studies were carried out and experimental results were reported in table. Galantamine was used as a control for its ability to inhibit both ChEs. The results of AChE inhibition revealed that all selected compounds showed moderate degree of inhibition with IC₅₀ values ranging from 126.94 to 183.51 μM. In terms of inhibitory activity against BChE, all the tested compounds gave very low BChE inhibition label with IC₅₀ values greater than 200 μM (**Table 4**).

Table 4

Cholinesterase inhibitory activities of selected compounds

| Compound | IC ₅₀ (μM) ± SD/% inhibition ^a | |
|--------------------------|--|------------|
| | AChE | BChE |
| 4c | 159.56±1.03 | >200 |
| 4d | 135.67±0.75 | >200 |
| 4h | 139.53±2.02 | >200 |
| 4i | 126.94±2.50 | >200 |
| 4m | 183.51±0.98 | >200 |
| Galantamine ^b | 21.82±4.00 | 40.72±2.85 |

^aIC₅₀ values represent the means ± SD of three parallel measurements (p < 0.05).

^bReference compound.

3.2.2. Antibacterial activity

The *in vitro* antibacterial activity of the synthesized derivatives was evaluated against six important bacterial strains from both gram positive and gram negative groups (**Fig. 1**).

Fig. 1. Histogram of the antimicrobial activity of compounds 4a-p

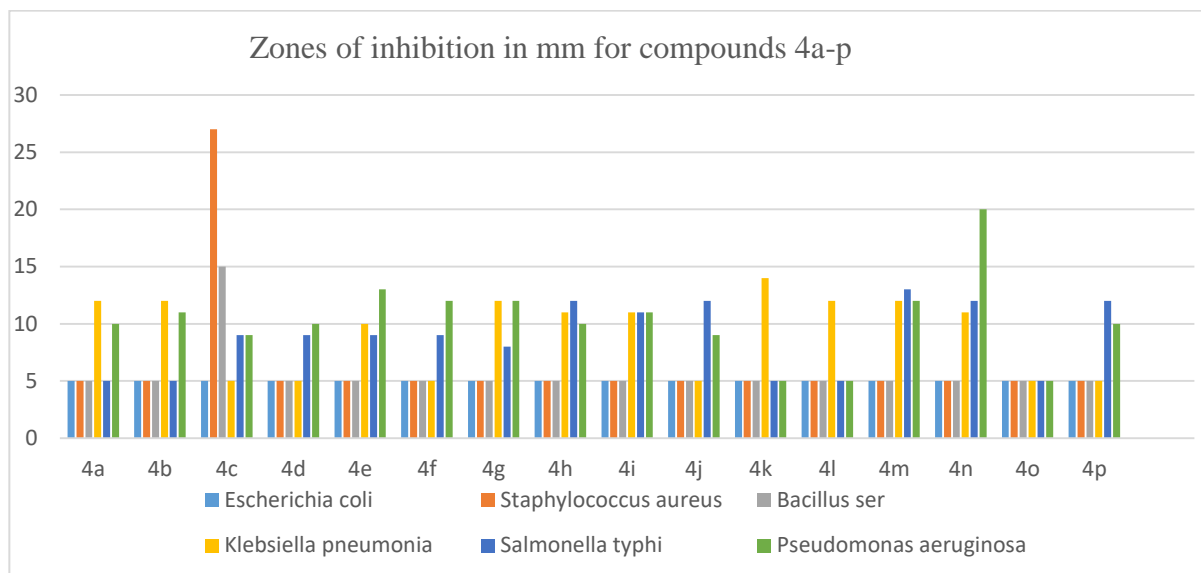
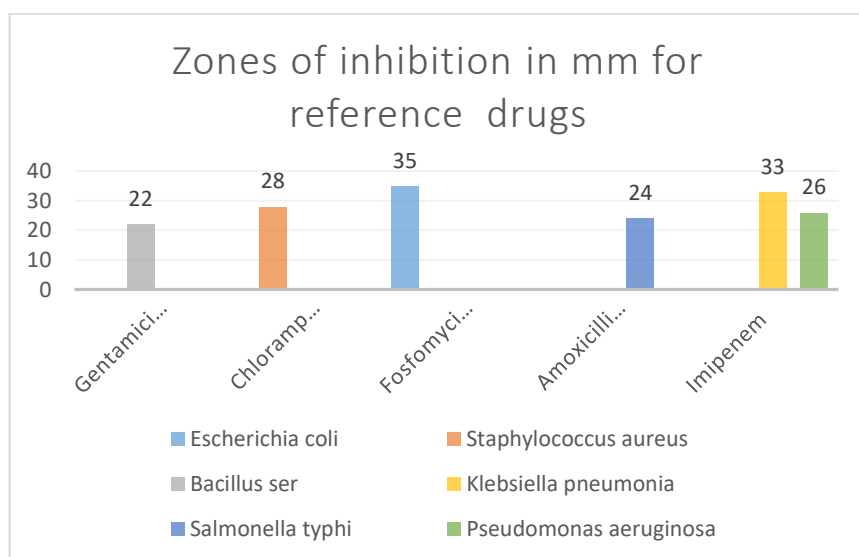


Fig. 2. Histogram of reference drugs



Most interestingly, the tested derivatives exhibited the highest activity on:

-*Staphylococcus aureus*, which compound **4c**, was the most potent one, with inhibition diameter equal to 27 mm, comparable to that of the reference drug (chloramphenicol 28 mm)

-*Bacillus cereus*, which compound **4c** with a zone of inhibition of 15 mm, was found to be the most potent compound. This compound was comparable to the reference drug gentamicin with a zone of inhibition of 22 mm.

-*Pseudomonas aeruginosa*, which compound **4n**, was found to be the most active compound in the series with a zone of inhibition of 20 mm comparable to the reference drug imipenem with a zone of inhibition of 26 mm.

Compounds of **4a**, **4b**, **4g**, **4k**, **4l** and **4m** had good activity against *Klebsiella pneumonia*, while the compounds of 4e, 4h, 4i and 4n had moderate activity. Compounds **4h**, **4m**, **4j**, **4n** and **4p** showed good zone of inhibition with *Salmonella typhi*, moderate activity with **4c**, **4d**, **4e**, **4f**, **4g** and **4i**. It was also observed that the compounds **4e**, **4f**, **4g** and **4m** had an important antibacterial activity against *Pseudomonas aeruginosa*, moderate activity with **4a**, **4b**, **4c**, **4d**, **4h**, **4i**, **4j** and **4p**. The **4o** compound had no activity against the six bacterial strains tested. Furthermore, no inhibition zone was observed with *Echerichia coli*. This bacterium is highly sensitive against fosfomycine (35 mm).

Table 5

MIC (mg/ml) of selected compounds

| compound | Antibacterial activity (MIC : mg/ml) | | |
|----------|--------------------------------------|------------------------|-------------------------------|
| | <i>Staphylococcus aureus</i> | <i>Bacillus Cereus</i> | <i>Pseudomonas aeruginosa</i> |
| 4c | 0.23 | 0.94 | - |
| 4n | - | - | 0.47 |

The minimum inhibition concentrations (MIC) were determined in liquid medium for the most active substances with different concentrations in decreasing order. The results are grouped in **Table 5**.

3.3. Theoretical investigations

3.3.1. Frontier molecular orbitals (FMOs)

To assess the structural properties and global reactivity descriptors, we analyzed the frontier molecular orbitals. These orbitals, known as the highest occupied molecular orbital (HOMO) and the lowest unoccupied molecular orbital (LUMO), serve as reliable indicators for determining the physical characteristics of molecules. Additionally, they provide essential insights into interactions with biological receptors and molecules [59]. The hardness of molecular species, determines their capability to resist electron acceptance. In theory, soft molecular species are expected to exhibit higher reactivity compared to hard molecules [59], the electronegativity (χ), hardness (η), softness (S), electronic chemical potential (μ), electrophilicity index (ω), Ionization Energy (IP) and Electron Affinity (EA), all of these values can be computed based on HOMO and LUMO energy levels. These calculations were carried out using the specified equations:

$$\eta = (E_{\text{LUMO}} - E_{\text{HOMO}})/2 \quad (1)$$

$$\mu = (E_{\text{HOMO}} + E_{\text{LUMO}})/2 \quad (2)$$

$$\omega = \mu^2/2\eta = -\chi \quad (3)$$

$$S = 1/2\eta \quad (4)$$

$$\text{IP} = -E_{\text{HOMO}} \quad (5)$$

$$\text{EA} = -E_{\text{LUMO}} \quad (6)$$

The aim is to gain insights into the chemical selectivity and reactivity of the studied molecules, the hardness of molecular species, determines their capability to resist electron acceptance. In theory, soft molecular species are expected to exhibit higher reactivity compared to hard molecules [60]. **Table 6** shows Global descriptors of compounds **4c**, **4n** and **4p**.

Table 6

Global descriptors of the studied compound.

| Compounds | HOMO | LUMO | Energy Gap | IP | EA | μ | ω | S | χ | η |
|-----------|-------|-------|------------|------|------|-------|----------|------|--------|--------|
| 4c | -6,48 | -2,37 | 4,11 | 6,48 | 2,37 | -4,42 | 4,76 | 0,24 | 4,42 | 2,10 |
| 4n | -5,96 | -1,88 | 4,08 | 5,96 | 1,88 | -3,92 | 3,77 | 0,24 | 3,92 | 2,04 |
| 4p | -6.26 | -1,89 | 4,37 | 6.26 | 1,89 | -4,08 | 3,80 | 0,23 | 4,08 | 2,18 |

The observed energy gap demonstrates a progressive increase in the following sequence: $4n < 4c < 4p$ (B, A) with values of $4.08 < 4.11 < 4.37$.

The FMOs of the three molecules are shown in Fig.1. The HOMO functions as the orbital donating electrons, while the LUMO acts as the orbital accepting electrons [61].

Fig. 3 shows that in compound **4p** the primary concentration of the highest occupied molecular orbital is located on the carbon atoms of the benzene and pyran rings, accounting for approximately 38% and 10.01%, respectively. Additionally, a significant presence is observed on the pair of nitrogen atoms, contributing approximately 20%. While the LUMO is mostly located in the pyran compound with formaldehyde ring.

Concerning the compound **4n**, the HOMO is spread across the atoms of furan ring 65% and 14% around the atoms of pyran ring, while the LUMO is mainly localized on the pyrone ring. Regarding compound **4c**, its electronic structure reveals a compelling pattern of molecular orbitals. Notably, the Highest Occupied Molecular Orbital (HOMO) showcases a prominent resonance with roughly 42% of its electron density encompassing the atoms constituting the pyran ring. Intriguingly, a contrasting 27% of the electronic density is dispersed across the Nitrogen atoms of the CN and NH₂ molecules. Conversely, the Lowest Unoccupied Molecular Orbital (LUMO) exhibits a distinct localization primarily focused on the NO₂ molecule, while approximately 14% extends to the benzene ring. This distinctive electronic distribution suggests a complex interplay of conjugation and electron delocalization within the compound potentially bearing significant consequences for its reactivity and electronic behavior.

These results affirm the stability of these compounds, enabling a comparison to be made with the band gap energy levels of biologically active substances [62].

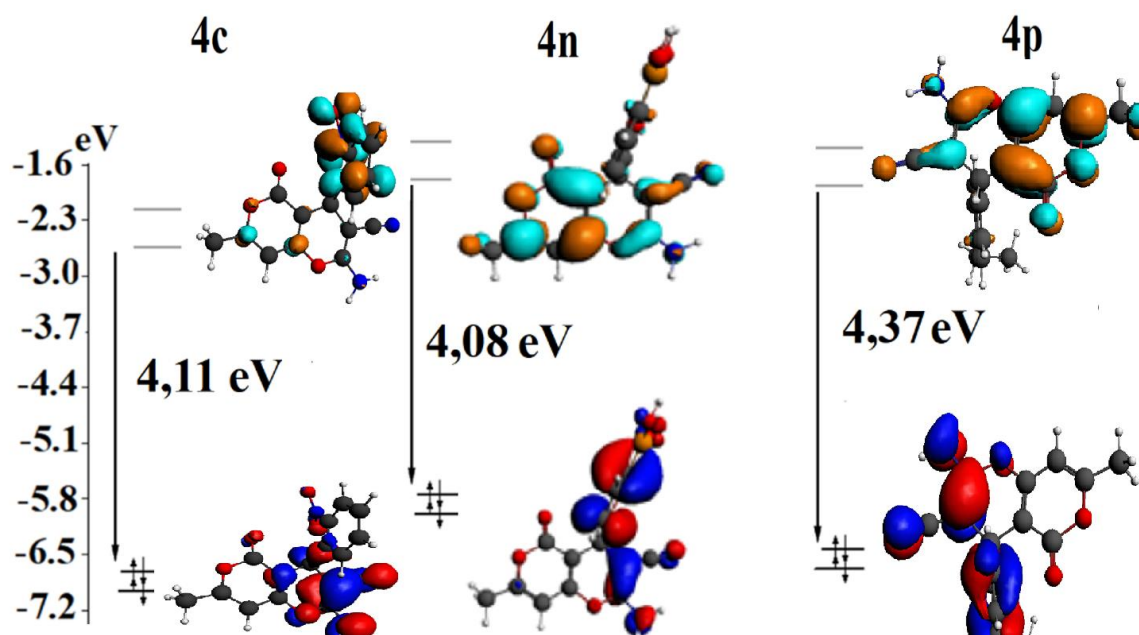


Fig. 3. HOMO-LUMO plots (ground state) and energy diagram. HOMO-LUMO plots of **4c**, **4n** and **4p**.

3.3.2. Vibrations Analysis

The IR spectra have been studied theoretically in the classical region 4000-400 cm^{-1} and as previously reported [63-66] the analysis of the vibrations allows us to have an idea about the electronic structure of a selected molecule.

For our part, vibration frequencies were computed utilizing the DFT approach. This computational method enabled the identification and understanding of each fixed position. The outcomes (illustrated in **Fig. 4**) demonstrated that, in the case of the two compounds, the lack of an imaginary spectrum verifies the stability and actuality of their geometry.

Fig. 4 illustrates the presence of uneven extension in C-H bonds across the spectral span of 3000 cm^{-1} to 3100 cm^{-1} , displaying bands of mild to moderate intensity for compounds **4c**, **4n** and **4p**. The computed wavenumbers at 3352–3563 cm^{-1} were identified as corresponding to the asymmetric and symmetric stretching vibrations of the N–H bond of NH_2 , respectively. On the other hand, the bands observed at 1638, 1598, 1564-1591 cm^{-1} in theoretical vibration spectra were attributed to the stretching vibrations of the C-C ring. C=O stretching vibration was observed at 1680 and 1740 cm^{-1} of the two molecules A and B respectively. Theoretical vibrational spectra displayed moderately to strongly pronounced bands at 2185–2195 cm^{-1} , which were attributed to the stretching vibration of $\text{C}\equiv\text{N}$ bonds. The peak of A at 3646 cm^{-1} is due to the stretching of the O-H.

Our investigation yielded a noteworthy discovery, pinpointing angular deformation, or bending, vibrations within the CH bonds. These vibrations were precisely identified within the calculated wave number range of 1200 to 1440 cm^{-1} . This finding stands as a pivotal augmentation to our comprehension of the compound's intricate molecular dynamics and structural intricacies. Moreover, it harmoniously aligns with our comprehensive spectroscopic analysis, bolstering our efforts to achieve a thorough characterization of the compounds vibrational properties. Together, these insights provide a more nuanced and complete portrait of the compound's behavior at the molecular level.

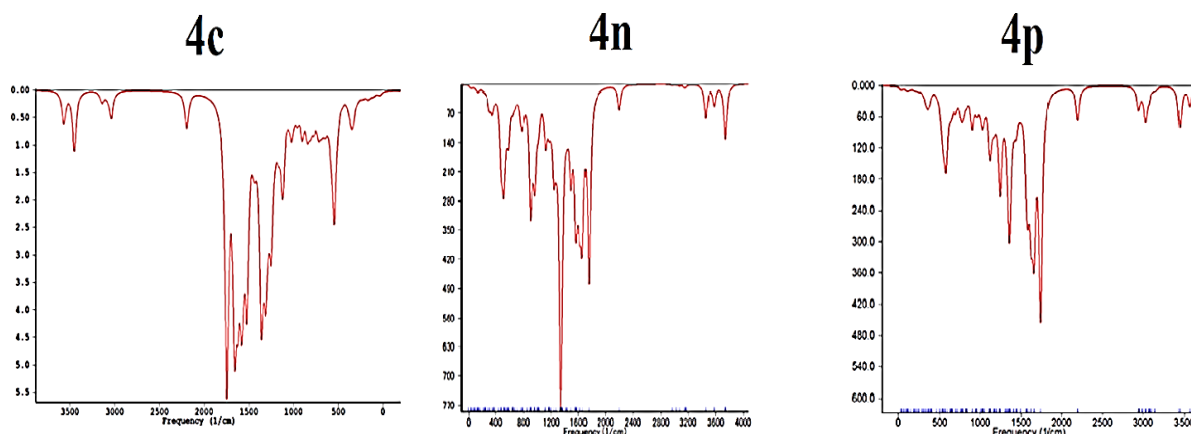


Fig. 4. Theoretical vibrational spectra of IR **4c**, **4n** and **4p**

3.3.3. Ultraviolet-Visible Spectral Analysis

UV–visible spectral was conducted, predicting the electronic transitions of the both molecules (**4c**, **4n** and **4p**). Simulation of the UV–vis spectrum was performed for the gaseous phase and provided in **Fig. 5**, the computed optical characteristics including excitation energy, excitation wavelength(λ), oscillator strength (f), and the respective orbital contributions with their Assignment for the electronic transition are outlined in **Table 7**.

As illustrated in **Fig. 5**, the TD-DFT analysis spectra divulge that these compounds share a common absorption range, marked by absorption features at approximately 180-420 nm. Notably, three distinct absorption bands stand out: one at around 212 nm (with energy $E \approx 5.73\text{eV}$) for **4c**, another at 241 nm ($E \approx 5.14\text{eV}$) for **4n**, and a third at 195 nm ($E \approx 6.36\text{ eV}$) for **4p**. These absorptions exhibit oscillator strengths of 0.05, 0.12, and 0.1, respectively. Within these excitations, the primary contributions stem from the H-7 \rightarrow L+2, H \rightarrow L+7, and H-4 \rightarrow L+5 configurations for **4c**, **4n**, and **4p**, respectively, involving $\pi \rightarrow \pi^*$ transitions.

Moreover, the absorption bands located at 250, 212 nm, and 217 nm in the compounds originate from distinct electronic transitions: $\pi \rightarrow \pi^*$, $\pi \rightarrow \pi^*$, and $n \rightarrow \pi^*$. These transitions can be attributed to specific electronic configurations - the H-8 \rightarrow L+1 transition for the absorption at 250 nm, the H-11 \rightarrow L transition for the absorption at 212 nm, and the H-11 \rightarrow L+3 transition for the absorption at 217 nm.

This detailed analysis sheds light on the precise nature of electronic excitations occurring within these compounds, contributing to a deeper understanding of their optical characteristics.

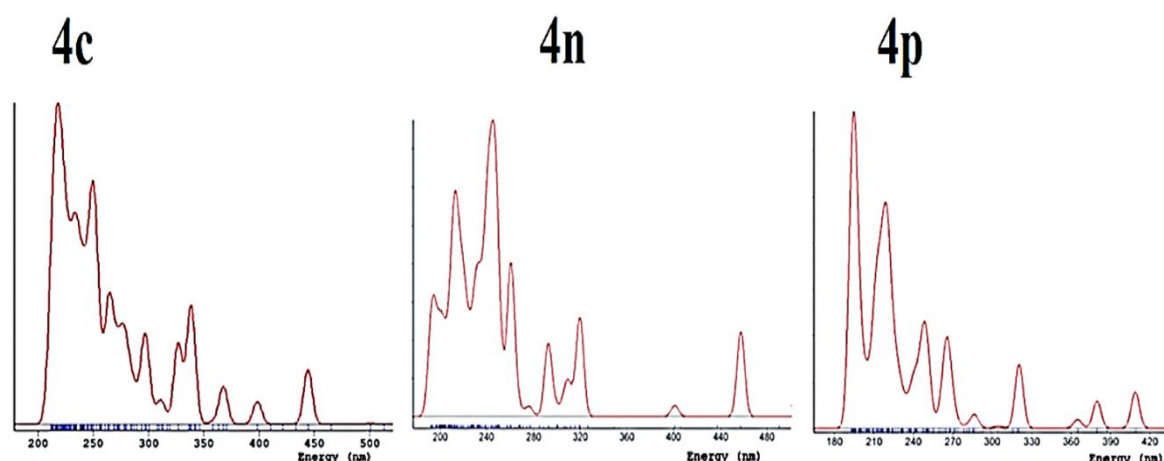


Fig. 5. Theoretical UV-vis absorption spectra of **4c**, **4n** and **4p**

Table 7

The computed optical characteristics UV-vis. Spectral parameters for molecules **4n**, **4p**, **4n**

| λ (nm) | f | E (eV) | Orbital contributions | | Assignment |
|----------------|------|--------|-----------------------|-----|-------------------------|
| 4c | | | | | |
| 3.46 | 0.05 | 3.66 | H-4→L | 67% | $\pi \rightarrow \pi^*$ |
| 250 | 0.08 | 4.97 | H-8→L+1 | 27% | $\pi \rightarrow \pi^*$ |
| 2.12 | 0.05 | 5.73 | H-8→L+1 | 27% | $\pi \rightarrow \pi^*$ |
| 4n | | | | | |
| 260 | 0.12 | 4.76 | H-2→L+1 | 27% | $\pi \rightarrow \pi^*$ |
| 241 | 0.12 | 5.14 | H→L+7 | 29% | $\pi \rightarrow \pi^*$ |
| 212 | 0.08 | 5.84 | H-11→L | 40% | $\pi \rightarrow \pi^*$ |
| 4p | | | | | |
| 409 | 0.04 | 3.03 | H→L | 95% | $\pi \rightarrow \pi^*$ |
| 380 | 0.03 | 3.26 | H-1→L | 63% | $\pi \rightarrow \pi^*$ |
| 321 | 0.07 | 3.86 | H-3→L | 42% | $\pi \rightarrow \pi^*$ |
| 217 | 0.03 | 5.71 | H-11→L+3 | 38% | $\pi \rightarrow \pi^*$ |
| 195 | 0.10 | 6.36 | H-5→L+3 | 50% | $\pi \rightarrow \pi^*$ |

3.3.4. MESP analysis

The molecular electrostatic potential serves as a crucial tool in illustrating and visually portraying variations in charge distribution within a molecule. This technique aids in the identification of sites prone to electrophilic and nucleophilic reactions, as well as the detection of hydrogen-bonding interactions [67-70], various colors depict distinct electrostatic potential values on the surface.

Fig.6 illustrates the electrostatic potential of the compounds, ranging from -0.0565 to 0.556.

In the graphical representation, the blue portion indicates a positive MESP, the red segment represents a negative electrostatic potential (ESP), and the green area corresponds to neutrality, light blue indicates a slightly electron-deficient area, yellow denotes a slightly electron-rich. Analyzing the MESP surface diagram in Figure 6 reveals a concentration of negative regions (depicted in red) primarily around the oxygen and nitrogen atoms in both molecules, exhibit nucleophilic characteristics. In contrast, positive regions are distributed around the hydrogen atoms, serving as binding sites for electrophilic reactive entities.

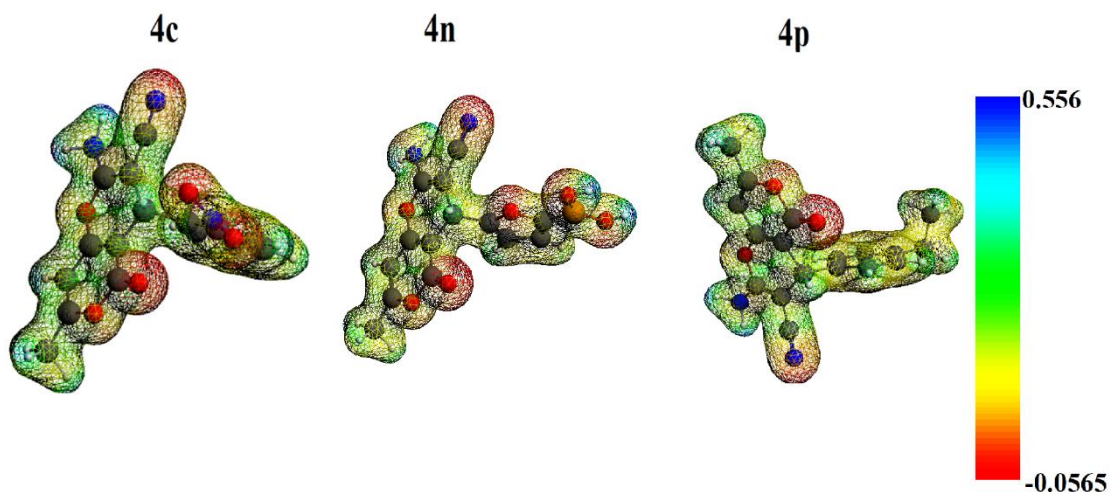


Fig. 6. Molecular electrostatic potential surface of, **4c**, **4n** and **4p**

3.3.5. Docking results

Molecular docking is used to understand biological reactions and try to predict the synthesis of potentially active molecules. This is a simulation process that predicts the structure and conformation of a receptor-ligand molecular complex which is generally a protein-molecule complex [71-73].

Antimicrobial are crafted to disrupt of bacterial metabolism, targeting their critical structures. These targeted assaults aim to dismantle the fundamental processes necessary for bacterial survival and proliferation.

In this study, the dynamic interplay between the target receptors and the ligand was scrutinized with precision using the potent tool of Discovery Studio Visualizer. The focus was primarily on the conformations that exhibited the lowest free binding energy.

This strategic approach enabled a comprehensive assessment of the binding interactions, shedding light on the strength and stability of the molecular associations within the active site, and the outcomes are displayed in **Table 8**, **Fig. 5** and **6** show the binding interaction of **4c** with target proteins.

As illustrated in **Fig. 7**, **4c** was positioned in the active site with binding energy values (-5.8 and -5.6 kcal/mol).

The compound **4c** demonstrated similar residual interactions with specific amino acid residues of the 1gym target receptors, including Lys-201, Tyr200, His32, Ser-236, His-82, Trp-47, Pro-245, Arg-69. Additionally, it formed one hydrogen bond with Trp-47 and van der waals interaction (VDW) with His-82, Pro-245, Arg-69 (see **Fig. 7**). In contrast, when interacting with the target receptor 5BS3, **4c** displayed distinct patterns. Here, it established residual interactions with amino acid residues G-10, Met-1121, Ser-1084, Asp-1083, Ala-1120, while forming one hydrogen bond with nucleophile G F-10, π Anion with amino acids Asp-1083 and π Sulfur with Met-1121 (see **Fig. 8**). This differential binding profile suggests that **4c** interacts with the two receptors in distinct yet specific ways, potentially leading to varying biological responses or efficacy in inhibiting their respective targets.

Table 8

The interaction characteristics of the studied compound with *Bacillus cereus* and *Staphylococcus aureus* (1gym and 5bs3)

| Protein | Binding affinity (Ligand) kcal/mol | Amino acid residue |
|---------|------------------------------------|--|
| 1gym | -5.8 | Lys-201, Tyr200, His32, Ser-236, His-82, Trp-47, Pro-245, Arg-69 |
| 5bs3 | -5.6 | G-F10, Met-1121, Ser-1084, Asp-1083, Ala-1120 |

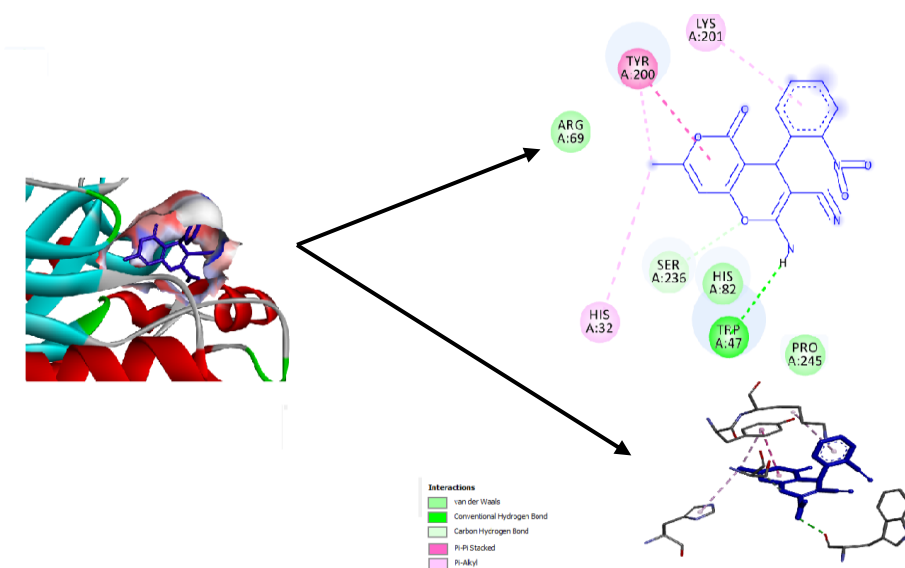


Fig. 7. Docked view of the Compound **4c** at the active site of *Bacillus cereus* (PDB ID: 1GYM).

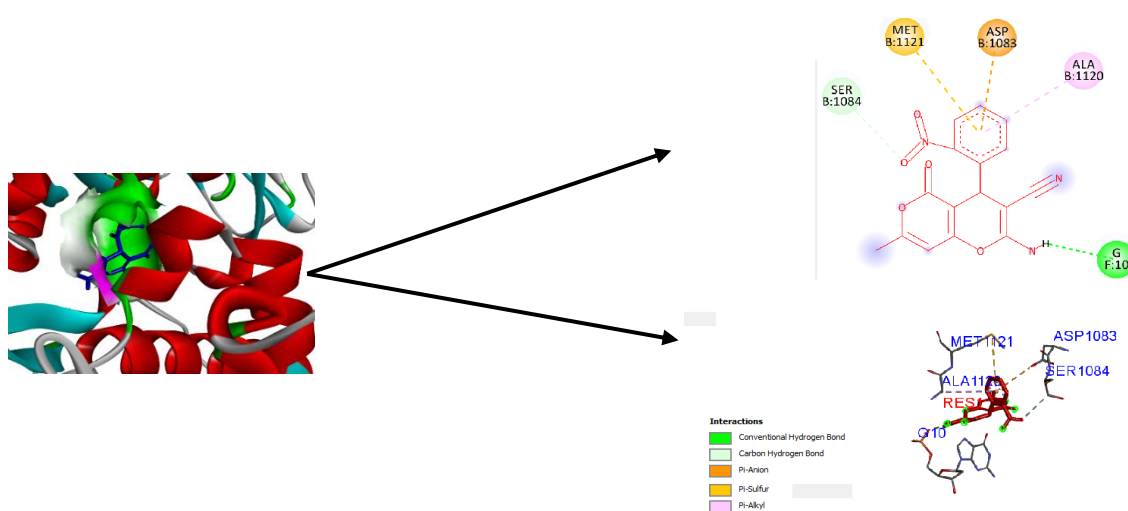


Fig. 8. Docked view of the Compound **4c** at the active site of *Staphylococcus aureus* (PDB ID: 5bs3)

3.3.6. The ADME-Toxicity and Pass Analysis

A number of web-based software applications, namely SwissADME (the webpage (<http://www.swissadme.ch>), ADMETlab 2.0, and PASS Online, were pinpointed for conducting toxicity investigations. These software solutions are extensively employed within

the realm of computational toxicology and have undergone validation to accurately prognosticate the toxicity of chemical compounds [74,75].

An effective pharmaceutical candidate must demonstrate not only efficacy but also the capacity to reach its intended site within the body at the necessary concentration to carry out the expected biological function without inducing adverse effects. Consequently, the promising experimental results have been supplemented by a computational analysis of their ADMET properties.

Table 9 provides a summary of particular projected ADME results.

Table 9

Certain forecasted ADME characteristics of the Compounds

| | 4a | 4b | 4c | 4d | 4e | 4f | 4g | 4h |
|--------------------------|-----------|-----------|-----------|-----------|-----------|-----------|-----------|-----------|
| Physicochemical Property | | | | | | | | |
| MW | 280.08 | 314.05 | 325.07 | 325.07 | 325.07 | 310.10 | 310.10 | 294.10 |
| N-HA | 5 | 5 | 8 | 8 | 8 | 6 | 6 | 5 |
| N-HD | 1 | 1 | 1 | 1 | 1 | 1 | 1 | 1 |
| N-RB | 1 | 1 | 2 | 2 | 2 | 2 | 2 | 1 |
| TPSA | 87.08 | 87.08 | 130.22 | 130.22 | 130.22 | 96.31 | 96.31 | 87.08 |
| logS | -2.59 | -2.72 | -2.40 | -2.50 | -2.64 | -2.65 | -2.75 | -2.67 |
| Solubility Class | Soluble |
| logP | 1.63 | 2.41 | 1.55 | 1.69 | 1.680 | 1.529 | 1.71 | 2.09 |
| logD | 1.33 | 2.30 | 1.18 | 1.36 | 1.39 | 1.25 | 1.46 | 1.67 |
| Medicinal Chemistry | | | | | | | | |
| Fsp3 | 0.188 | 0.188 | 0.188 | 0.188 | 0.188 | 0.23 | 0.23 | 0.23 |
| Lipinski Rule | Suitable |
| Pfizer Rule | Yes |
| PAINS | 0 alert |
| Metabolism | | | | | | | | |
| CYP1A2 | No | Yes | No | No | No | No | No | Yes |

| | | | | | | | | |
|-------------------|-----|-----|-----|-----|-----|-----|-----|-----|
| inhibitor | | | | | | | | |
| CYP2C19 inhibitor | Yes | Yes | No | No | No | Yes | Yes | Yes |
| CYP3A4 inhibitor | No | No | No | No | No | Yes | Yes | No |
| CYP2C9 inhibitor | No | Yes |
| CYP2D6 inhibitor | No |
| BBB | No |
| HIA | Low |

| | 4i | 4j | 4k | 4l | 4m | 4n | 4o | 4p |
|--------------------------|----------|----------|----------|----------|----------|----------|----------|----------|
| Physicochemical Property | | | | | | | | |
| MW | 294.10 | 294.10 | 286.04 | 296.08 | 270.08 | 314.07 | 324.09 | 308.12 |
| N-HA | 5 | 5 | 5 | 6 | 7 | 8 | 7 | 5 |
| N-HD | 1 | 1 | 1 | 2 | 2 | 3 | 3 | 1 |
| N-RB | 1 | 1 | 1 | 1 | 1 | 2 | 2 | 2 |
| TPSA | 87.08 | 87.08 | 87.08 | 107.31 | 115.76 | 140.68 | 127.54 | 87.08 |
| logS | -2.81 | -2.81 | -2.39 | -2.65 | -2.48 | -2.087 | -2.26 | -2.84 |
| Solubility Class | Soluble |
| logP | 2.14 | 2.15 | 1.36 | 1.21 | -0.26 | -0.148 | 0.17 | 2.595 |
| logD | 1.72 | 1.78 | 1.14 | 1.03 | -0.45 | 0.58 | 0.85 | 2.50 |
| Medicinal Chemistry | | | | | | | | |
| Fsp3 | 0.235 | 0.235 | 0.214 | 0.188 | 0.231 | 0.214 | 0.188 | 0.278 |
| Lipinski Rule | Suitable |
| Pfizer Rule | Yes |
| PAINS | 0 alert |
| Metabolism | | | | | | | | |
| CYP1A2 inhibitor | Yes | Yes | Yes | No | No | No | No | Yes |
| CYP2C19 | Yes | Yes | Yes | No | No | No | No | Yes |

| | | | | | | | | |
|------------------|-----|-----|------|-----|-----|------|------|------|
| inhibitor | | | | | | | | |
| CYP3A4 inhibitor | No | No | No | No | No | No | No | No |
| CYP2C9 inhibitor | Yes | Yes | Yes | No | No | No | No | Yes |
| CYP2D6 inhibitor | No | No | No | No | No | No | No | No |
| BBB | No | No | No | No | No | No | No | No |
| HIA | Low | Low | High | Low | Low | High | High | High |

Table 9 continued

MW =Molecular Weight, N-HA=Num. H-bond Acceptors, N-HD=Num. H-bond donors, N-RB=Num. rotatable bonds, Fsp3 =Fraction Csp3 acceptors, HIA= Human Intestinal Absorption, CYP= Cytochrome P450, BBB = Blood-Brain Barrier, PAINS=Pan Assay Interference compounds or frequent hitters or promiscuous Compounds

3.3.7. Physical and chemical characteristics

According to the **Table 8**, the physico-chemical properties of the investigated compounds were assessed following the Lipinski guidelines, meeting the criteria for selection and confirming their favorable bioavailability. Evaluating the LogP values, all falling within the specified range of -2 to 5, indicates their strong solubility potential in the body's aqueous environments

3.3.8. Pharmacokinetic propriety

According to **Table 9** the blood-brain barrier (BBB) is impermeable to all compounds, all compounds showed a high possibility of gastrointestinal absorption (HIA). Furthermore, the Swiss model provides the capability to predict whether a compound functions as an inhibitor of cytochrome P450 (CYP) isoenzymes, pivotal for drug biotransformation.

Among the scrutinized compounds 4(L-O), none demonstrated inhibitory effects on cytochrome P450 isoenzymes, a contrast to the remaining molecules, which exhibit inhibition towards at least one CYP isoenzyme, Initially, this inhibition doesn't appear to have any negative impacts on the metabolism. Fortunately, we observe that CYP3A4 remains unaffected, except when it comes to the substances **4g** and **4f**.

3.3.9. PASS Analysis

To anticipate additional biological effects of the provided molecules, a technique called PASS analysis was employed. PASS online utilizes the molecules structures to estimate its biological activities. The PASS program generates an output consisting of a list of anticipated activity types, along with the associated probabilities of being "active" (Pa) or "inactive" (Pi). These Pa and Pi values are independent and span from 0 to 1.

When Pa exceeds 0.7, there is a high likelihood of observing the predicted activity in experimental tests. However, this might result in the identification of compounds closely resembling known drugs. For Pa values between 0.5 and 0.7, the probability of detecting an experimental activity is reduced. Yet, if such predictions are validated, the discovered compound could serve as the foundational structure for a novel chemical class pertaining to the studied biological activity.

Numerous authors have confirmed PASS predictions through subsequent synthesis and biological testing, yielding promising outcomes.

The proposed tasks for compounds with a strong likelihood are outlined in **Table 10**. With Pa surpassing 0.7 for the projected activities, the compounds have the potential to demonstrate these effects in practical experiments. Yet, the intended activities are based on probability and necessitate experimental validation. Virtually all compounds exhibit activity as an inducer of apoptosis, as an inhibitor of cystinyl aminopeptidase and Hepatic disorders treatment except some compounds.

Table 10

Some biological activities of molecule predicted by PASS

| Pa | Pi | Activity | Compounds |
|-------|-------|-----------------------------------|-----------|
| 0,774 | 0,009 | Apoptosis agonist | 4o |
| 0,765 | 0,002 | Cystinyl aminopeptidase inhibitor | |
| 0,808 | 0,008 | Apoptosis agonist | 4n |
| 0,685 | 0,003 | Cystinyl aminopeptidase inhibitor | |
| 0,696 | 0,003 | Cystinyl aminopeptidase inhibitor | 4m |
| 0,542 | 0,034 | Apoptosis agonist | |
| 0,817 | 0,002 | Cystinyl aminopeptidase inhibitor | 4l |
| 0,815 | 0,007 | Apoptosis agonist | |
| 0,634 | 0,005 | Hepatic disorders treatment | |

| | | | |
|-------|-------|-----------------------------------|-----------|
| 0,707 | 0,003 | Cystinyl aminopeptidase inhibitor | 4k |
| 0,668 | 0,018 | Apoptosis agonist | |
| 0,824 | 0,001 | Cystinyl aminopeptidase inhibitor | 4j |
| 0,805 | 0,008 | Apoptosis agonist | |
| 0,639 | 0,005 | Hepatic disorders treatment | |
| 0,808 | 0,002 | Cystinyl aminopeptidase inhibitor | 4i |
| 0,785 | 0,009 | Apoptosis agonist | |
| 0,615 | 0,005 | Hepatic disorders treatment | |
| 0,808 | 0,002 | Cystinyl aminopeptidase inhibitor | 4h |
| 0,796 | 0,008 | Apoptosis agonist | |
| 0,637 | 0,005 | Hepatic disorders treatment | |
| 0,807 | 0,008 | Apoptosis agonist | 4g |
| 0,798 | 0,002 | Cystinyl aminopeptidase inhibitor | |
| 0,607 | 0,006 | Hepatic disorders treatment | |
| 0,799 | 0,008 | Apoptosis agonist | 4f |
| 0,784 | 0,002 | Cystinyl aminopeptidase inhibitor | |
| 0,646 | 0,005 | Hepatic disorders treatment | |
| 0,797 | 0,002 | Cystinyl aminopeptidase inhibitor | 4e |
| 0,756 | 0,010 | Apoptosis agonist | |
| 0,574 | 0,008 | Hepatic disorders treatment | |
| 0,782 | 0,002 | Cystinyl aminopeptidase inhibitor | 4d |
| 0,732 | 0,012 | Apoptosis agonist | |
| 0,549 | 0,009 | Hepatic disorders treatment | |
| ,782 | 0,002 | Cystinyl aminopeptidase inhibitor | 4c |
| 0,744 | 0,011 | Apoptosis agonist | |
| 0,581 | 0,007 | Hepatic disorders treatment | |
| 0,806 | 0,002 | Cystinyl aminopeptidase inhibitor | 4b |
| 0,753 | 0,011 | Apoptosis agonist | |
| 0,836 | 0,001 | Cystinyl aminopeptidase inhibitor | 4a |
| 0,672 | 0,005 | Hepatic disorders treatment | |
| 0,796 | 0,002 | Cystinyl aminopeptidase inhibitor | 4p |
| 0,750 | 0,011 | Apoptosis agonist | |
| 0,586 | 0,007 | Hepatic disorders treatment | |

3.4. Crystal structure analysis

Single-crystal structure analysis shows that the crystal structure has been described in monoclinic symmetry and $C 2/c$ centric space group ($R_{\text{int}} = 0.1231$). Cell parameters have been refined as follows: $a = 21.776(4) \text{ \AA}$, $b = 8.1486(14) \text{ \AA}$, $c = 18.492(3) \text{ \AA}$, $\beta = 106.573(5)^\circ$ and $V = 3145.0(9) \text{ \AA}^3$. The number of formula unit $Z = 8$, and calculated density d and absorption coefficient μ values are 1.302 g.cm^{-3} and 0.090 mm^{-1} , respectively.

The complete crystallographic data for **4p** are presented in **table 11**. The molecule **4p** presents an a priori dynamic disorder at the level of the C19- C22 bond (C22A, C22B). The C19-C22 bond makes a movement of 8.4° around the bisector of the angle C19-C22A-C22B. The two pyran rings form an angle of $2.14 (1)^\circ$. The angle between the mean planes of benzene and [4,3-*b*]pyran is $83.49(2)^\circ$. None of the methyl hydrogens H3A, H3B, and H3C are contained within the mean plane of benzene and [4,3-*b*]pyran is $83.49(2)^\circ$.

The endocyclic angles in the para position of the benzene ring C18-C19-C20,

C17-C16-C21 present a $1.3(4)^\circ$ difference. The bond lengths of the benzene ring atoms in para

position C19 and C16 linked respectively to the butane radical and to [4, 3-*b*] pyran do not show

significant differences [C19- C22A(C22B) = 1.55 (2)Å] and C16-C15 = 1.53(4)Å (**Fig. 9**).

Intramolecular hydrogen bonds N11-H11A...O6 [2.950 (4)Å] and N11-H11B... N14 [3.080(4)Å] are formed between the pyran rings competing to ensure cohesion in the crystal (Table 12) symmetry code: x, y, z, -x+1/2, -y+1/2, -z. The molecules generate infinite zig-zags along the b-axis (**Fig. 10**). The molecules are linked via π - π stacking amid the pyran rings. The distance between the centroids of the pyran (C1-O4-C2-C7-C8-C5) and (C7-O9-C8-C10-C12-C15) ring is 4.096(3) Å.

Table 11

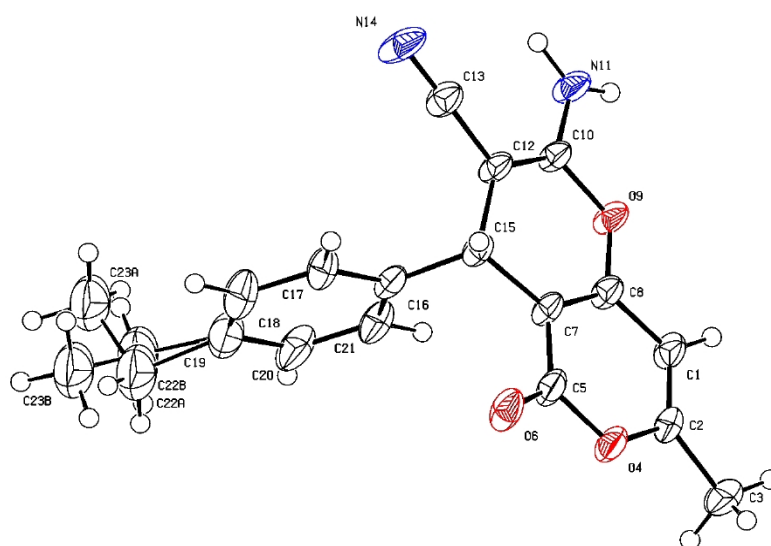
Single-crystal X-ray data and structure refinement details for **4p**.

| | |
|---|--|
| Crystal data | |
| Chemical formula | C ₁₈ H ₁₆ N ₂ O ₃ |
| <i>M_r</i> | 308.33 |
| Crystal system, space group | Monoclinic, <i>C2/c</i> |
| Temperature (K) | 150 |
| <i>a</i> , <i>b</i> , <i>c</i> (Å) | 21.776 (4), 8.1486 (14), 18.492 (3) |
| β (°) | 106.573 (5) |
| <i>V</i> (Å ³) | 3145.0 (9) |
| <i>Z</i> | 8 |
| Radiation type | Mo <i>K</i> α |
| μ (mm ⁻¹) | 0.09 |
| Crystal size (mm) | 0.17 × 0.12 × 0.02 |
| Data collection | |
| Diffractometer | D8 VENTURE Bruker AXS |
| Absorption correction | Multi-scan [Sheldrick, G.M. (2014). <i>SADABS</i> Bruker AXS Inc., Madison, Wisconsin, USA] |
| <i>T_{min}</i> , <i>T_{max}</i> | 0.821, 0.998 |
| No. of measured, independent and observed reflections [<i>I</i> > 2 σ (<i>I</i>)] | 17531, 3620, 1907 |
| <i>R_{int}</i> | 0.123 |
| (sin θ/λ) max (Å ⁻¹) | 0.651 |
| Refinement | |
| <i>R</i> [<i>F</i> ² > 2 σ (<i>F</i> ²)], <i>wR</i> (<i>F</i> ²), <i>S</i> | 0.089, 0.220, 1.04 |
| No. of reflections | 3620 |
| No. of parameters | 215 |
| H-atom treatment | H atoms treated by a mixture of independent and constrained refinement |
| $\Delta\rho_{\max}$, $\Delta\rho_{\min}$ (e Å ⁻³) | 0.36, -0.47 |

Table 12

Hydrogen-bond geometry (Å, °)

| D—H...A | D—H | H...A | D...A | D—H...A |
|---|----------|----------|-----------|---------|
| N11—H11A...O6i | 0.94 (4) | 2.02 (4) | 2.950 (4) | 170 (4) |
| N11—H11B...N14ii | 0.89 (4) | 2.19 (4) | 3.080 (4) | 178 (4) |
| Symmetry codes: (i) $x, y-1, z$; (ii) $-x+3/2, -y+1/2, -z+1$. | | | | |

**Fig. 9.** The molecular structure of **4p** with the atom labelling and displacement ellipsoids drawn at the 50% probability level.

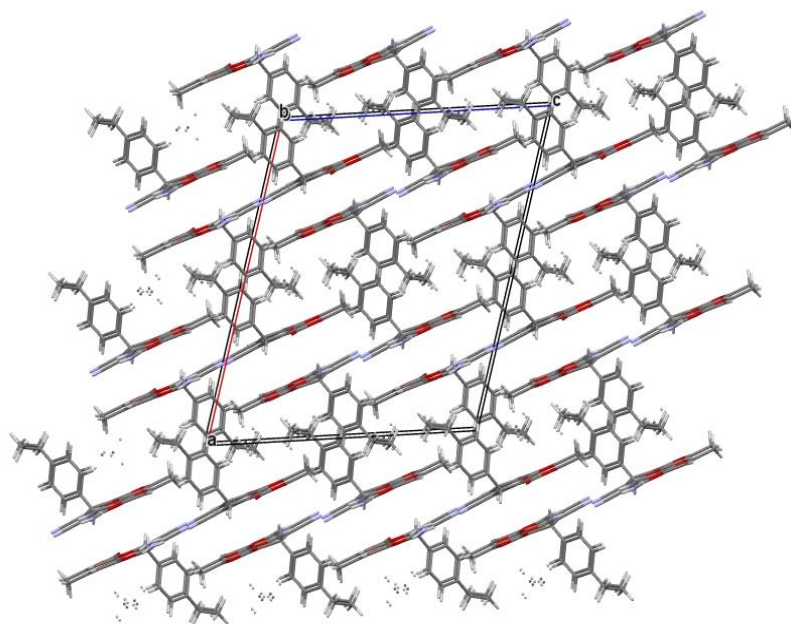


Fig. 10. A view along the b-axis of the Crystal packing

3.5. Hirshfeld surface analysis (HS), 2D fingerprint plot, energy and energy framework

3.5.1. Hirshfeld surface analysis (HS)

By applying a three-dimensional Hirshfeld surface (HS) [76], we can understand crystal packing comprehensively and obtain valuable data on the interactions between each atom within the crystal structure. **Fig. 11** presents the distribution of the Hirshfeld surface of compound **4p** ($C_{18}H_{16}N_2O_3$) mapped over d_{norm} from -0.5057 to 1.4361. This mapping was accomplished using CrystalExplorer2 [76] and the Crystallographic Information File (CIF) data. In this colour range, red corresponds to contacts close to the van der Waals radii, blue signifies contacts exceeding the van der Waals radii, and white indicates contacts equivalent to the van der Waals radii. Hirshfeld surfaces are rendered transparently to allow the visualisation of the underlying molecular components of the compound. On HS, there are 14 red spots, degraded from dark-red, medium-red, and light-red spots, where the dark-red spots represent the H...H, C...H, N - H... N and N - H... O short contacts, medium-red spots represent N...C and N...H, light-red spots represent C...C contacts in methyl groups, and π - π stacking. The Shape Index from -0.5057 to 1.4361 was used to visualise the π - π stacking as adjacent blue and red triangles [71-73] (**Fig. 12a**). Curvedness in the range of -4.0000 to 0.4000 presented in Fig. 2b by large green planes separated by dark blue edges [77]. Fragment Patches from 0.0000 to 13.0000 refer to the surface patches adjacent to neighbouring surfaces [72]. The electrostatic potential (**Fig. 13**) was determined using the TONTO program, integrated within CrystalExplorer21, by choosing the Hartree-Fock function with STO-3G basis from -0.0500 to 0.0500. The regions coloured in red and blue correspond to negative and positive electrostatic potentials, respectively [78].

3.5.2. The 2D fingerprint plot

The 2D fingerprint plot serves as a tool to accentuate specific atomic pair interactions. This facilitates quantifying the individual influence exerted by each interaction, considering the diverse types of interactions implicated in the structural modification [79]. In the fingerprint, there are corresponding areas where one molecule predominantly functions as a donor ($d_e > d_i$) while the other molecule primarily serves as an acceptor ($d_i > d_e$) (**Table 13**). presents the 2D fingerprint plot illustrating various intermolecular interactions of **4p**, along with a pie chart showing the percentage contributions of these interactions in the Hirshfeld surface. The most substantial contribution, accounting for 45.8% with $d_e + d_i = 1.8 \text{ \AA}$, is attributed to the H...H contact (**Fig. 14a, Fig. 14k**). The C...H/H...C interactions represent the second most significant contribution in the 2D fingerprint plot (**Fig. 14b, Fig. 14k**), accounting for 18.7% and concentrated on the periphery with $d_e + d_i = 2.8 \text{ \AA}$. The H...O/O...H interaction consists of two spikes with a contribution of 17.0% and $d_e + d_i = 1.9 \text{ \AA}$ (**Fig. 14c**). The H...N/N...H interactions represent a contribution of 11.6 % with $d_e + d_i = 2 \text{ \AA}$ (**Fig. 14d**). The fingerprint of C...O/O...C is $d_e + d_i = 3.4 \text{ \AA}$ with a contribution of 3.2 % (**Fig. 14e**). C...N/N...C interactions cover only 1.3% of the surface with $d_e + d_i = 3.3 \text{ \AA}$ (**Fig. 14f**). The contribution of O...O is 0.8% with $d_e + d_i = 3.4 \text{ \AA}$ (**Fig. 14g**). The C...C interactions concentrate on the middle with a contribution of 0.7 % and $d_e + d_i = 3.2 \text{ \AA}$ (**Fig. 14h**). The contribution of N...N interactions is 0.5% with $d_e + d_i = 3.0 \text{ \AA}$ (**Fig. 14i**). The minor substantial contribution, accounting for 0.3 % with $d_e + d_i = 3.4 \text{ \AA}$, is attributed to the O...N/N...O contact (**Fig. 14j, Fig. 14k**).

3.5.3. Energy and energy framework

The interaction energy between molecules can be broken down into four main components: electrostatic interactions, polarisation effects, dispersion forces, and exchange repulsion [76]. These energy components were determined using the wavefunctions HF/3-21G. The total interaction energy was determined for a molecular cluster with a radius of 3.8 \AA centred around the molecule of interest (**Fig. 15a**). with scale factors of $K_{\text{ele}}=1.019$, $K_{\text{dis}}=0.651$, $K_{\text{rep}}=0.901$ [80]. The results revealed that the dispersion energy is the most significant component (**Table 14**). The most important interaction among the neighbouring molecules is between the central molecule and the symmetry-bound molecule at $-x$, $-y$, $-z$ (coloured lime). The energy values for this interaction are as follows: Electrostatic energy (E_{ele}) is -20.8 kJ/mol , Polarization energy (E_{pol}) is -4.7 kJ/mol , Dispersion energy (E_{dis}) is -71.5 kJ/mol , Repulsion energy (E_{rep}) is 47.1 kJ/mol , and the total energy (E_{tot}) is -47.1 kJ/mol . Energy frameworks are utilised to graphically depict the intensities of intermolecular interaction energies, thereby providing a visual interpretation of the supramolecular architecture of the crystal structure. The interaction energies between molecular pairs are symbolised by cylinders connecting the centroids of the molecule pairs. The radius of these cylinders is proportional to the intensity of the interaction energy. The frameworks are designed with red cylinders for E_{elec} , green for E_{dis} , and blue for E_{tot} (refer to **Figures 5b–5d**). These cylinders illustrate the relative strength of molecular packing in different directions [81].

Table 23

Percentage of the contribution of intermolecular interactions to the Hirshfeld surface of the title compound

| Contacts | Contribution % | Contacts | Contribution % |
|-------------|----------------|-------------|----------------|
| C...C | 0.7 | H...O/O...H | 17.0 |
| C...H/H...C | 18.7 | H...N/N...H | 11.6 |
| C...O/O...C | 3.2 | O...O | 0.8 |
| C...N/N...C | 1.3 | N...N | 0.5 |
| H...H | 45.8 | O...N/N...O | 0.3 |

Table 14

Interaction energies (kJ mol⁻¹) between a reference molecule and its neighbours. N is the number of equivalent neighbours, and R is the distance between molecular centroids (mean atomic position) in Å.

| | N | Symop | R | E_ele | E_pol | E_dis | E_rep | E_tot |
|--|---|-----------------------|-------|-------|-------|-------|-------|-------|
| | 0 | -x+1/2, y+1/2, -z+1/2 | 7.79 | -3.1 | -4.5 | -34.9 | 11.8 | -27.9 |
| | 0 | x, y, z | 8.15 | -34.4 | -12.1 | -15.7 | 18.3 | -42.3 |
| | 0 | -x, -y, -z | 6.00 | -20.8 | -4.7 | -71.5 | 47.1 | -50.5 |
| | 0 | x, -y, z+1/2 | 9.54 | -4.9 | -7.5 | -32.0 | 13.7 | -27.6 |
| | 0 | -x, y, -z+1/2 | 8.59 | 1.9 | -2.5 | -20.1 | 7.9 | -11.4 |
| | 0 | -x+1/2, -y+1/2, -z | 9.97 | -69.9 | -20.5 | -14.1 | 44.1 | -61.6 |
| | 0 | -x+1/2, -y+1/2, -z | 7.82 | -4.0 | -7.6 | -22.1 | 25.3 | -8.4 |
| | 0 | -x, y, -z+1/2 | 12.57 | 0.0 | -22.7 | 0.0 | 0.0 | -14.7 |
| | 0 | -x, -y, -z | 8.01 | 13.4 | -15.9 | -68.8 | 78.6 | 5.0 |
| | 0 | x, -y, z+1/2 | 10.91 | -16.6 | -4.0 | -14.6 | 12.4 | -22.6 |

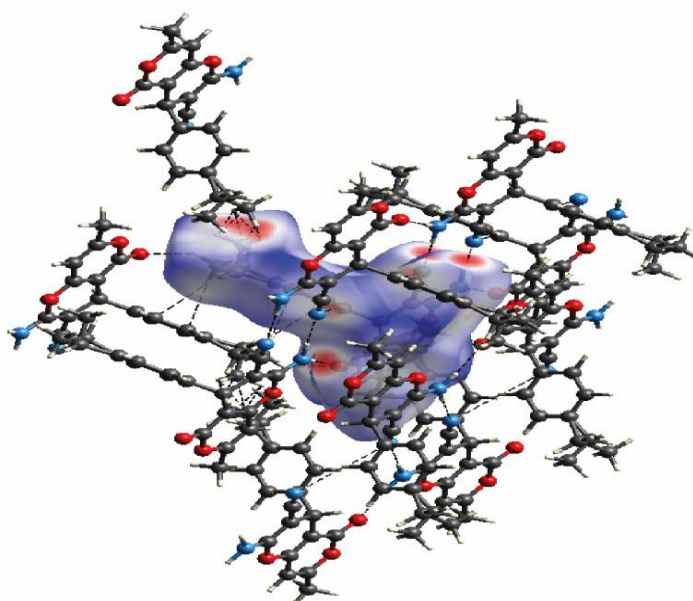


Fig. 11. Hirshfeld surface mapped over d_{norm} for **4p** along the b-axis.

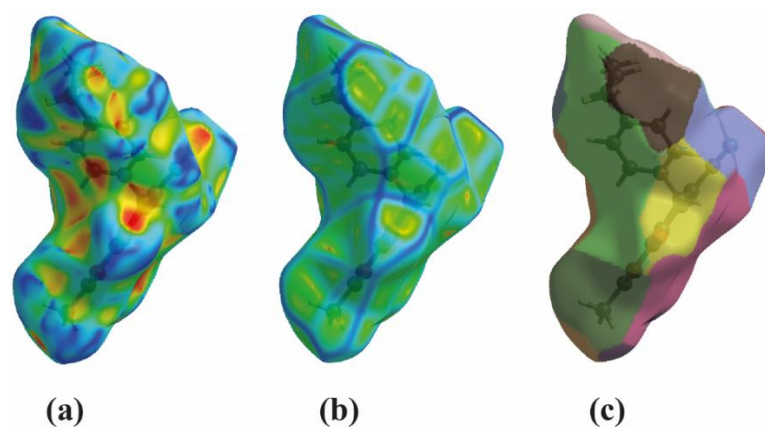


Fig. 12. (a) Shape Index, (b) Curvedness and (c) Fragment Patch along the b-axis

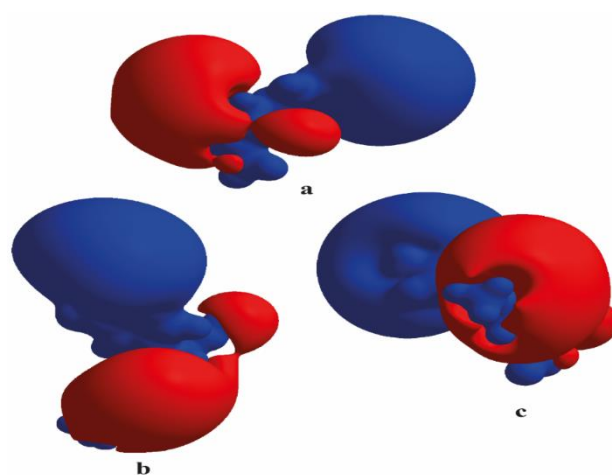


Fig. 13. Electrostatic potential mapped along a, b and c axes.

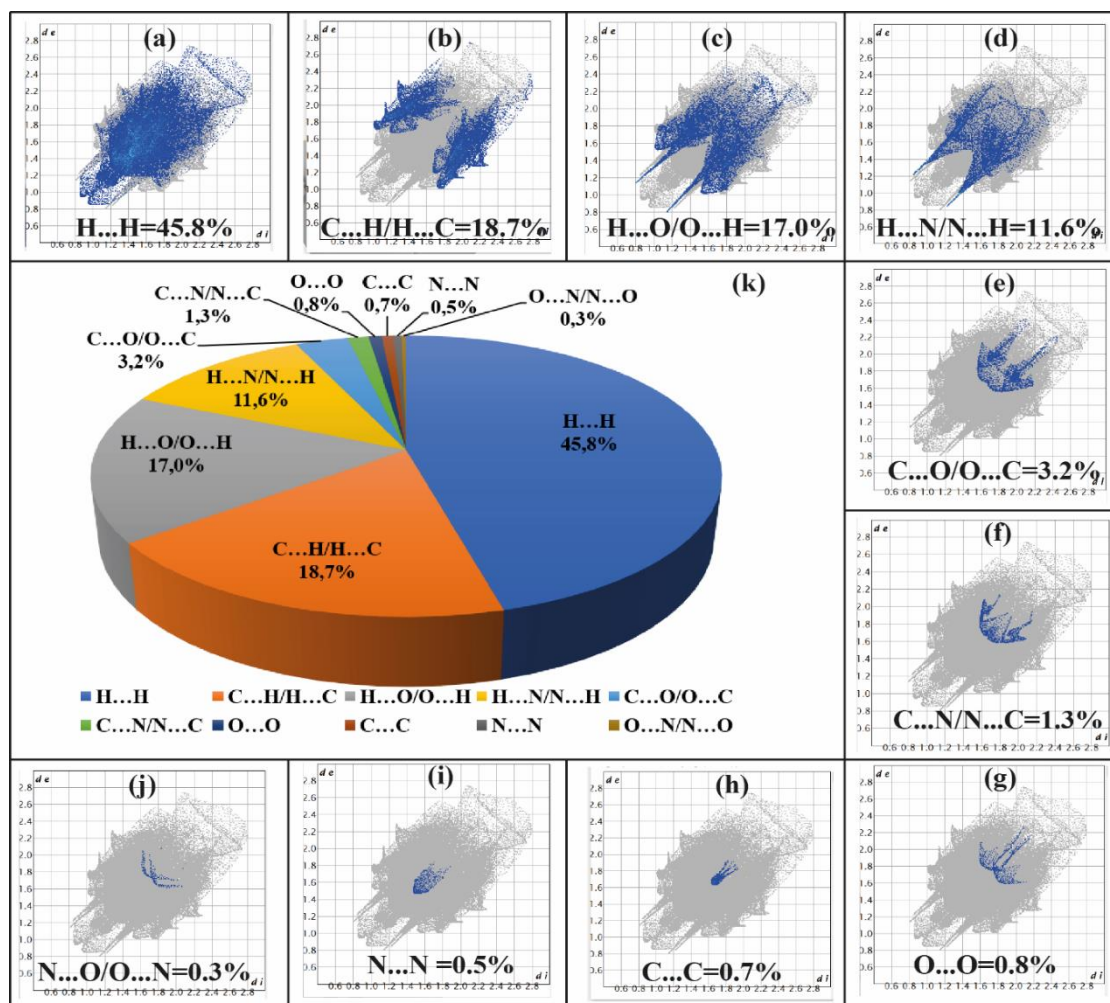


Fig. 14. Two-dimensional fingerprint plots for **4p** showing the contributions of different types of interactions: (a) H...H, (b) C...H/H...C, (c) H...O/O...H, (d) H...N/N...H, (e) C...O/O...C, (f) C...N/N...C, (g) O...O, (h) C...C, (i) N...N, (j) N...O/O...N, (k) Pie chart representing the percentage contributions of different interactions in the Hirshfeld surface.

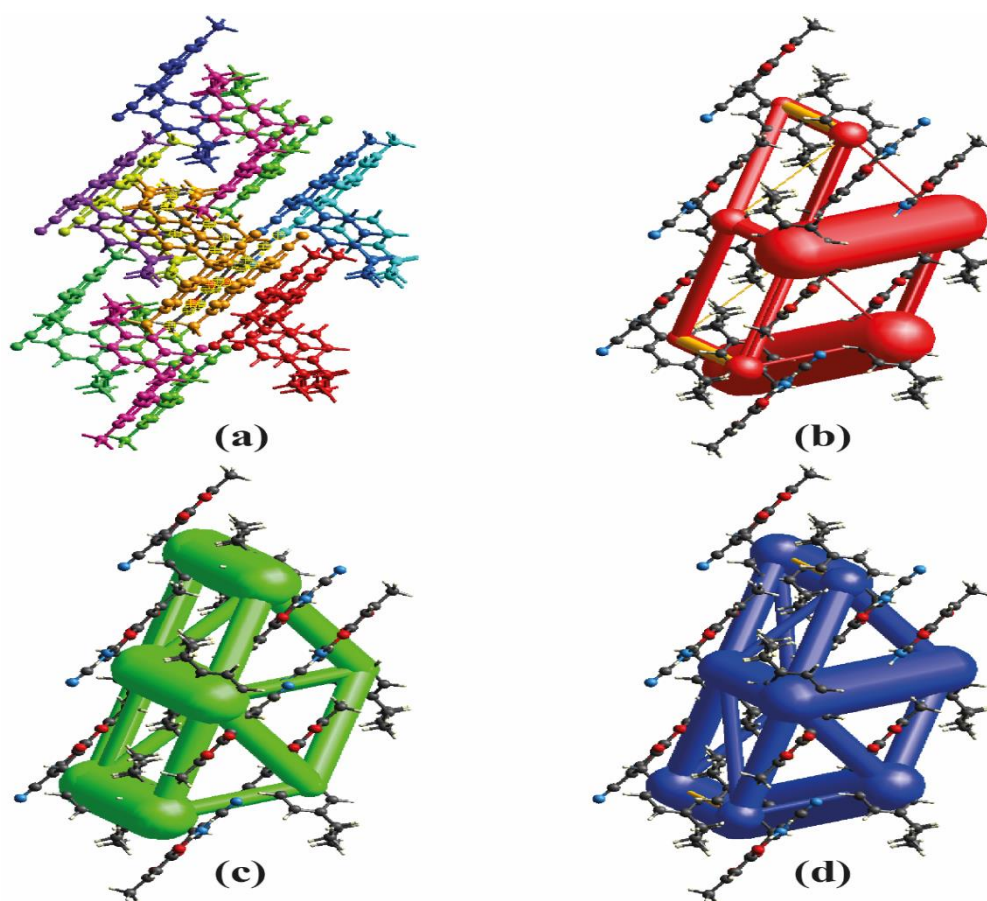


Fig. 15. (a) Interactions between the reference molecule and the molecules present in a 3.8 Å cluster around, (b) Energy frameworks built for E_{cle} (red cylinders), (c) Energy frameworks built for E_{dis} (green cylinders), (d) Energy frameworks built for E_{tot} (blue cylinders) along the c-axis.

4. Conclusion

In the present work, we describe a new procedure for the preparation of pyrano[4,3b]pyran derivatives (**4a-p**) by the three-component reaction between 4-hydroxy-6-methylpyran-2-one, malononitrile and a variety of aromatic and heteroaromatic aldehydes catalyzed by pyridinium *p*-toluenesulfonate. The reactions are carried out at reflux of an H₂O/EtOH mixture in the presence of 10 mol% of catalyst and the expected compounds are obtained with very good yields which vary between 76 and 95% in just 0.25 hour. The molecular structures of the synthesized compounds were confirmed by ¹H and ¹³C NMR and high-resolution HRMS mass spectroscopy and for the compound **4p** by X-ray diffraction analysis and its Hirshfeld surface analyzed. The AChE and BChE inhibitory activities of a few selected molecules were evaluated and the results are weak. Furthermore, the antibacterial activity of the synthesized compounds was also evaluated against six bacteria and some of them showed interesting results, sometimes higher than the reference product. Additionally, an in-depth theoretical study was carried out including DFT calculations, IR, UV-visible vibration, MESP, ADME-Toxicity analysis, molecular docking as well as pharmacokinetic properties.

Conflict of interest

The authors declare that they have no known competing financial interests or personal relationships that could have appeared to influence the work reported in this paper.

Acknowledgements

The authors gratefully acknowledge le Ministère de l'Enseignement Supérieur et de la Recherche Scientifique (Algeria) for the financial support.

Références

- [1] A. Laurent, C. F. Gerhardt, Ueber einige stickstoffverbindungen des benzoyls. *Ann Chim Phys.* (1838) vol. 66, p. 181-181.
- [2] A. Strecker, Ueber die künstliche Bildung der Milchsäure und einen neuen, dem Glycocoll homologen Körper;, *Justus Liebigs Ann. Chem.* 75 (1850) 27–45. <https://doi.org/10.1002/jlac.18500750103>.
- [3] M. Seifi, H. Sheibani, High surface area MgO as a highly effective heterogeneous base catalyst for three-component synthesis of tetrahydrobenzopyran and 3,4-dihydropyrano[c] chromene derivatives in aqueous media, *Catal. Letters.* 126 (2008) 275–279. <https://doi.org/10.1007/s10562-008-9603-5>.
- [4] J.M. Khurana, B. Nand, P. Saluja, DBU: a highly efficient catalyst for one-pot synthesis of substituted 3,4-dihydropyrano[3,2-c]chromenes, dihydropyrano[4,3-b]pyranes, 2-amino-4H-benzo[h]chromenes and 2-amino-4H benzo[g]chromenes in aqueous medium, *Tetrahedron.* 66 (2010) 5637–5641. <https://doi.org/10.1016/J.TET.2010.05.082>.
- [5] D. Rajguru, B.S. Keshwal, S. Jain, Solvent-free, green and efficient synthesis of pyrano[4, 3-b]pyrans by grinding and their biological evaluation as antitumor and antioxidant agents, *Med. Chem. Res.* 22 (2013) 5934–5939. <https://doi.org/10.1007/s00044-013-0586-4>.
- [6] M.N. Elinson, R.F. Nasybullin, G.I. Nikishin, Electrocatalytic Efficient Multicomponent Approach to Medicinally Relevant Pyrano[4,3-b]pyran Scaffold, *Electrocatalysis.* 4 (2013) 56–60. <https://doi.org/10.1007/s12678-012-0119-9>.
- [7] D. Rajguru, B.S. Keshwal, S. Jain, $H_6P_2W_{18}O_{62} \cdot 18H_2O$: A green and reusable catalyst for one-pot synthesis of pyrano[4,3-b]pyrans in water, *Chinese Chem. Lett.* 24 (2013) 1033–1036. <https://doi.org/10.1016/j.ccllet.2013.07.010>.
- [8] M.A. Zolfigol, M. Yarie, S. Bagheri, A. Khoshnood, D.A. Alonso, 1H-imidazol-3-ium tricyanomethanide {[HIM]C(CN)₃} as a nanostructured molten salt catalyst: application to the synthesis of pyrano[4,3-b]pyrans, *Res. Chem. Intermed.* 43 (2017) 3291–3305. <https://doi.org/10.1007/s11164-016-2826-y>.
- [9] P.P. Mohire, D.R. Chandam, R.B. Patil, D.R. Kumbhar, S.J. Jadhav, A.A. Patravale, V.P. Godase, J.S. Ghosh, M.B. Deshmukh, Protic Ionic Liquid Promoted One Pot Synthesis of 2-amino-4-(phenyl)-7-methyl-5-oxo-4H,5H-pyrano[4,3-b]pyran-3-carbonitrile Derivatives in Water and Their Antimycobacterial Activity, *J. Heterocycl.*

- Chem. 55 (2018) 1010–1023. <https://doi.org/10.1002/jhet.3133>.
- [10] N.G. Khaligh, T. Mihankhah, M.R. Johan, Synthesis of new low-viscous sulfonic acid-functionalized ionic liquid and its application as a Brønsted liquid acid catalyst for the one-pot mechano-synthesis of 4H-pyrans through the ball milling process, *J. Mol. Liq.* 277 (2019) 794–804. <https://doi.org/10.1016/j.molliq.2019.01.024>.
- [11] N.G. Khaligh, O.C. Ling, T. Mihankhah, M.R. Johan, J.J. Ching, 1,1'-Butylenebis(3-sulfo-3H-imidazol-1-ium) hydrogensulfate: a versatile task-specific ionic liquid catalyst for the synthesis of 4H-pyran scaffolds through non-conventional process, *Monatshefte Fur Chemie.* 150 (2019) 655–662. <https://doi.org/10.1007/s00706-018-2336-2>.
- [12] E. Mosaddegh, A. Hassankhani, Preparation and characterization of nano-CaO based on eggshell waste: Novel and green catalytic approach to highly efficient synthesis of pyrano [4, 3-b]pyrans, *Cuihua Xuebao/Chinese J. Catal.* 35 (2014) 351–356. [https://doi.org/10.1016/s1872-2067\(12\)60755-4](https://doi.org/10.1016/s1872-2067(12)60755-4).
- [13] M. Ghashang, S.S. Mansoor, K. Aswin, Thiourea dioxide: An efficient and reusable organocatalyst for the rapid one-pot synthesis of pyrano[4, 3-b]pyran derivatives in water, *Cuihua Xuebao/Chinese J. Catal.* 35 (2014) 127–133. [https://doi.org/10.1016/S1872-2067\(12\)60727-X](https://doi.org/10.1016/S1872-2067(12)60727-X).
- [14] N.G. Khaligh, S.B.A. Hamid, S.J.J. Titinchi, Succinimide-N-sulfonic Acid as a Recyclable Brønsted Acid Catalyst for Synthesis of Pyrano[4,3-b]pyran Derivatives by Using Solar Energy Under Solvent-Free Conditions, *Polycycl. Aromat. Compd.* 37 (2017) 31–38. <https://doi.org/10.1080/10406638.2015.1076010>.
- [15] L. Chen, J. Lin, B. Chen, L. Zhao, Sodium ethylene diamine tetraacetate catalyzed synthesis of chromene derivatives via multi-component reactions at low catalyst loading, *Res. Chem. Intermed.* 43 (2017) 6691–6700. <https://doi.org/10.1007/s11164-017-3015-3>.
- [16] X. Chen, W. Zhang, F. Yang, C. Guo, Z. Zhao, D. Ji, F. Zhou, Z. Wang, R. Zhao, L. Wang, Synthesis of dihydropyrano[4,3-b]pyranes via a multi-component reaction catalyzed by lipase, *Green Chem. Lett. Rev.* 10 (2017) 54–58. <https://doi.org/10.1080/17518253.2017.1285442>.
- [17] D. Tahmassebi, J.E. Blevins, S.S. Gerardot, Zn(L-proline) 2 as an efficient and reusable catalyst for the multi-component synthesis of pyran-annulated heterocyclic compounds, *Appl. Organomet. Chem.* 33 (2019) 1–11. <https://doi.org/10.1002/aoc.4807>.
- [18] W. Ma, A.G. Ebadi, M.S. Sabil, R. Javahershenas, G. Jimenez, One-pot synthesis of 2-amino-4: H -chromene derivatives by MNPs@Cu as an effective and reusable magnetic nanocatalyst, *RSC Adv.* 9 (2019) 12801–12812. <https://doi.org/10.1039/c9ra01679a>.
- [19] N.G. Khaligh, T. Mihankhah, M. Rafie Johan, 4,4'-Trimethylenedipiperidine (TMDP): An Efficient Organocatalyst for the Mechano-synthesis of Pyrano[4,3-b]pyrans under Solid-state Conditions, *Polycycl. Aromat. Compd.* 40 (2020) 1606–1615. <https://doi.org/10.1080/10406638.2018.1564679>.
- [20] S. Mousavi Khatat, B. Sadeghi, M. Ghasemi, Nano-cell- OBF_2 : an efficient and cheap catalyst for one-pot synthesis of pyrano[4,3-b]pyrans under mild and green condition, *Inorg. Nano-Metal Chem.* 49 (2019) 56–62.

<https://doi.org/10.1080/24701556.2019.1603159>.

- [21] N.G. Khaligh, T. Mihankhah, M.R. Johan, Catalytic Application of 1,4-Piperazinediethanesulfonic Acid (PIPES) for the One-pot Multicomponent Synthesis of Pyrano[4,3-b]pyrans, *Org. Prep. Proced. Int.* 52 (2020) 368–373. <https://doi.org/10.1080/00304948.2020.1761228>.
- [22] F. Matloubi Moghaddam, M. Eslami, G. Hoda, Cysteic acid grafted to magnetic graphene oxide as a promising recoverable solid acid catalyst for the synthesis of diverse 4H-chromene, *Sci. Rep.* 10 (2020) 1–14. <https://doi.org/10.1038/s41598-020-77872-8>.
- [23] F. Mohajer, F. Soltani HasanKiadeh, G. Mohammadi Ziarani, M. Zandiyeh, A. Badiei, R.S. Varma, Greener assembly of Pyrano[3,4-b]pyran derivative as a novel Hg²⁺ ion chemosensor, *Opt. Mater.* X. 15 (2022) 100182. <https://doi.org/10.1016/j.omx.2022.100182>.
- [24] M. Ziyaadini, N. Nemat-Bakhsh, S.J. Roudbaraki, M. Ghashang, Zn₂SnO₄-SnO₂ Nano-Composite Promoted Ultrasonic-Assisted Synthesis of Pyran Derivatives, *Polycycl. Aromat. Compd.* 42 (2020) 1-15. <https://doi.org/10.1080/10406638.2020.1743328>.
- [25] A. Ram Kumar, S. Selvaraj, P. Anthoniammal, R. Jothi Ramalingam, Ranjith Balu, P. Jayaprakash, G.P. Sheeja, Comparison of spectroscopic, structural, and molecular docking studies of 5-nitro-2-fluoroaniline and 2-nitro-5-fluoroaniline: An attempt on fluoroaniline isomers, *J. Fluor. Chem.*, 270 (2023) 110167, <https://doi.org/10.1016/j.jfluchem.2023.110167>.
- [26] A. Ram Kumara, C. Senthamil Selvib, S. Selvarajc, G. P. Sheeja Mold, P. Jayaprakashe, In Silico Studies on the Molecular Geometry, FMO, Mulliken Charges, MESP, ADME and Molecular Docking Prediction of Pyrogallol Carboxaldehydes as Potential Antitumour Agents, *Phys. Chem. Res.*, 12, (2024) 305-320. Doi : 10.22036/PCR.2023.402835.2359.
- [27] Z. Breijyeh, R. Karaman, Comprehensive Review on Alzheimer's Disease: Causes and Treatment. *Molecules*, 25 (2020), 5789; doi:10.3390/molecules25245789.
- [28] M.D. Aytemir, Ü. Çaliş, M. Özalp, Synthesis and evaluation of anticonvulsant and antimicrobial activities of 3-hydroxy-6-methyl-2-substituted 4H-pyran-4-one derivatives, *Arch. Pharm. (Weinheim)*. 337 (2004) 281–288. <https://doi.org/10.1002/ardp.200200754>.
- [29] X. Fan, D. Feng, Y. Qu, X. Zhang, J. Wang, P.M. Loiseau, G. Andrei, R. Snoeck, E. De Clercq, Practical and efficient synthesis of pyrano[3,2-c]pyridone, pyrano[4,3-b]pyran and their hybrids with nucleoside as potential antiviral and antileishmanial agents, *Bioorganic Med. Chem. Lett.* 20 (2010) 809–813. <https://doi.org/10.1016/j.bmcl.2009.12.102>.
- [30] T. Gale, Z. Zhang, Y. Liu, L. Panb, Novel pyran derivatives: Synthesis and anticancer activity in the bones, *Main Group Chem.* 17 (2018) 317–323.
- [31] I. Sehout, R. Boulcina, B. Boumoud, T. Boumoud, A. Debache, Solvent-free synthesis of polyhydroquinoline and 1,8-dioxodecahydroacridine derivatives through the Hantzsch reaction catalyzed by a natural organic acid: A green method, *Synth. Commun.* 47 (2017) 1185–1191. <https://doi.org/10.1080/00397911.2017.1316406>.

- [32] R. Laroum, R. Boulcina, C. Bensouici, A. Debache, Facile Synthesis and Antioxidant Evaluation of 4-Arylmethylideneisoxazol-5(4H)-ones, *Org. Prep. Proced. Int.* 51 (2019) 583–588. <https://doi.org/10.1080/00304948.2019.1677993>.
- [33] K. Boudebbous, H. Boulebd, C. Bensouici, D. Harakat, R. Boulcina, A. Debache, Synthesis, Docking Study and Biological Activities Evaluation of 1-Amidoalkyl-2-naphthol Derivatives as Dual Inhibitors of Cholinesterase and α -Glucosidase, *ChemistrySelect.* 5 (2020) 5515–5520. <https://doi.org/10.1002/slct.202000558>.
- [34] A. Ziadi Chibane, R. Boulcina, H. Boulebd, C. Bensouici, M. Yildirim, A. Debache, Green one-pot multicomponent synthesis, biological evaluation and theoretical investigations of some novel β -acetamido ketone derivatives as potent cholinesterase inhibitors, *Tetrahedron.* 76 (2020) 131260. <https://doi.org/10.1016/j.tet.2020.131260>.
- [35] M. Medimagh, N. Issaoui, S. Gatfaoui, O. Al-Dossary, A. S. Kazachenco, H. Marouani, Molecular modeling and biological activity analysis of new organic-inorganic hybrid: 2-(3,4-dihydroxyphenyl) ethanaminium nitrate, *J. King Saud Univ. Sci.*, 33 (2021) 101616.
- [36] A. Jumabaev, U. Holikulov, H. Hushvaktov, N. Issaoui, A. Absanov, Intermolecular interactions in ethanol solution of OABA: Raman, FTIR, DFT, M062X, MEP, NBO, FMO, AIM, NCI, RDG analysis, *J. Mol. Liq.* 377 (2023) 121552
- [37] O. Noureddine, N. Issaoui, S. Gatfaoui, O. Al-Dossary, H. Marouani, Quantum chemical calculations, spectroscopic properties and molecular docking studies of a novel piperazine derivative, *J. King Saud Univ. Sci.*, 33 (2021)101283.
- [38] A. S. Kazachenko, N. Issaoui, A. Sagaama, Y. N. Malyar, O. Al-Dossary, L. G. Bousiakou, A. S. Kazachenko, A. V. Miroshnokova, Z. Xiang, Hydrogen bonds interactions in biuret-water clusters: FTIR, X-ray diffraction, AIM, DFT, RDG, ELF, NLO analysis, derivative, *J. King Saud Univ. Sci.*, 34 (2022) 102350.
- [39] C. Bouregghda, I. Amine Khodja, B. Carboni, R. Boulcina, O. Kermiche, A. Debache, A Facile One-Pot and Green Multi-Component Synthesis of 2-Amino-4*H*-pyrans Promoted by Pyridinium *p*-Toluenesulfonate in Aqueous Medium, *Lett. Org. Chem.* 13 (2016) 482-490.
- [40] S. Mahdjoub, C. Derabli, R. Boulcina, G. Kirsch, A. Debache, Design and synthesis of novel 2-hydroxy-1,4-benzoxazine derivatives through three-component Petasis reaction catalysed by pyridinium toluene-sulphonate, *J. Chem. Res.* 40 (2016) 449–452. <https://doi.org/10.3184/174751916X14656634976813>.
- [41] R. Laroum, A. Debache, New eco-friendly procedure for the synthesis of 4-arylmethylene-isoxazol-5(4H)-ones catalyzed by pyridinium *p*-toluenesulfonate (PPTS) in aqueous medium, *Synth. Commun.* 48 (2018) 1876–1882. <https://doi.org/10.1080/00397911.2018.1473440>.
- [42] G.L. Ellman, K.D. Courtney, V. Andres, R.M. Featherstone, A new and rapid colorimetric determination of acetylcholinesterase activity, *Biochem. Pharmacol.* 7 (1961) 88–95. [https://doi.org/10.1016/0006-2952\(61\)90145-9](https://doi.org/10.1016/0006-2952(61)90145-9).
- [43] F.D. Gonelimali, J. Lin, W. Miao, J. Xuan, F. Charles, M. Chen, S.R. Hatab, Antimicrobial properties and mechanism of action of some plant extracts against food pathogens and spoilage microorganisms, *Front. Microbiol.* 9 (2018) 1–9. <https://doi.org/10.3389/fmicb.2018.01639>.

- [44] S. Magaldi, S. Mata-Essayag, C. Hartung De Capriles, C. Perez, M.T. Colella, C. Olaizola, Y. Ontiveros, Well diffusion for antifungal susceptibility testing, *Int. J. Infect. Dis.* 8 (2004) 39–45. <https://doi.org/10.1016/j.ijid.2003.03.002>.
- [45] C. Valgas, S.M. De Souza, E.F.A. Smânia, A. Smânia, Screening methods to determine antibacterial activity of natural products, *Brazilian J. Microbiol.* 38 (2007) 369–380. <https://doi.org/10.1590/S1517-83822007000200034>.
- [46] S.S. Suner, M. Sahiner, A. Akcali, N. Sahiner, Functionalization of halloysite nanotubes with polyethyleneimine and various ionic liquid forms with antimicrobial activity, *J. Appl. Polym. Sci.* 137 (2020) 1–10. <https://doi.org/10.1002/app.48352>.
- [47] T. Yanai, D.P. Tew, N.C. Handy, A new hybrid exchange-correlation functional using the Coulomb-attenuating method (CAM-B3LYP), *Chem. Phys. Lett.* 393 (2004) 51–57. <https://doi.org/10.1016/j.cplett.2004.06.011>.
- [48] Y. Akinaga, S. Ten-no, Range-separation by the Yukawa potential in long-range corrected density functional theory with Gaussian-type basis functions, *Chem. Phys. Lett.* 462 (2008) 348–351. <https://doi.org/10.1016/j.cplett.2008.07.103>.
- [49] G. Nageswari, G. George, S. Ramalingam, M. Govindarajan, Electronic and vibrational spectroscopic (FT-IR and FT-Raman) investigation using ab initio (HF) and DFT (B3LYP and B3PW91) and HOMO/LUMO/MEP analysis on the structure of l-serine methyl ester hydrogen chloride, *Journal of Molecular Structure.* 1166 (2018) 422–441. <https://doi.org/10.1016/j.molstruc.2018.04.014>.
- [50] I. Jomaa, N. Issaoui, T. Roisnel, H. Marouani, Insight into non-covalent interactions in a tetrachlorocadmate salt with promising NLO properties: Experimental and computational analysis, *Journal of Molecular Structure*, 1242 (2021), <https://doi.org/10.1016/j.molstruc.2021.130730>.
- [51] E.J. Baerends, D.E. Ellis, P. Ros, Self-consistent molecular Hartree-Fock-Slater calculations I. The computational procedure, *Chem. Phys.* 2 (1973) 41–51. [https://doi.org/10.1016/0301-0104\(73\)80059-X](https://doi.org/10.1016/0301-0104(73)80059-X).
- [52] A. Eddehech, R. Rahier, D. Donnarumma, F. Rigano, A. Noiriél, A. Abousalham, F. Cacciola, L. Mondello, Z. Zarai, Development of a highly efficient oil degumming process using a novel phosphatidylinositol-specific phospholipase C enzyme from *Bacillus thuringiensis* PL14, *Food Biosci.* 53 (2023) 102579. <https://doi.org/10.1016/J.FBIO.2023.102579>.
- [53] J. Agwupuye, T. Gber, H. Edet, M. Zeeshan, S. Batool, O. E. Duke and G. E. Egbung, Molecular modeling, DFT studies and biological evaluation of methyl 2, 8-dichloro-1, 2-dihydroquinoline-3-carboxylate, *Chem. Phys.* 6 (2023) 100–146.
- [54] Dassault Systemes BIOVIA: Discovery studio visualizer 21.1.0.20298 (2020). 2021.
- [55] G. Xiong, Z. Wu, J. Yi, L. Fu, Z. Yang, C. Hsieh, M. Yin, X. Zeng, C. Wu, A. Lu, X. Chen, T. Hou, D. Cao, ADMETlab 2.0: An integrated online platform for accurate and comprehensive predictions of ADMET properties, *Nucleic Acids Res.* 49 (2021) W5–W14. <https://doi.org/10.1093/NAR/GKAB255>.
- [56] G. M. Sheldrick, SHELXT - Integrated space-group and crystal-structure determination, *Acta Crystallogr A*, vol. 71, no. 1, pp. 3–8, Jan. 2015, doi:

10.1107/S2053273314026370

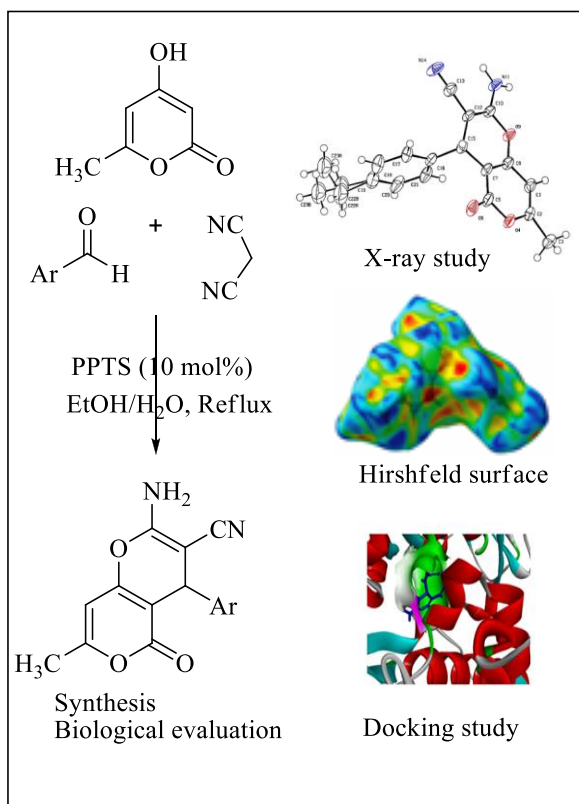
- [57] G. M. Sheldrick, Crystal structure refinement with SHELXL, *Acta Crystallogr. C Struct. Chem.*, 71 (2015) 3–8. doi: 10.1107/S2053229614024218
- [58] C. F. Macrae, P. R. Edgington, P. McCabe , E. Pidcock, G. P. Shields, R. Taylor, M. Towler, J. van de Streek, Mercury: Visualization and analysis of crystal structures, *J. Appl. Crystallogr.*, 39 (2006) 453–457. doi: 10.1107/S002188980600731X
- [59] R. Mohamed Asath, R. Premkumar, T. Mathavan, A. Milton Franklin Benial, Structural, spectroscopic and molecular docking studies on 2-amino-3-chloro-5-trifluoromethyl pyridine: A potential bioactive agent, *Spectrochim. Acta - Part A Mol. Biomol. Spectrosc.* 175 (2017) 51–60. <https://doi.org/10.1016/j.saa.2016.11.037>.
- [60] H. Louis, L. Guo, S. Zhu, S. Hussain, T. He, Computational study on interactions between CO₂ and (TiO₂)_n clusters at specific sites, *Chin. J. Chem. Phys.* 32 (6) (2019) 674–686.
- [61] A. Udoikono, H. Louis, E. Eno, E.C. Agwamba, T.O. Unimuke, A.T. Igbalagh, A.S. Adey, Reactive azo compounds as a potential chemotherapy drugs in the treatment of malignant glioblastoma (GBM): Experimental and theoretical studies, *J. Photochem. Photobiol. A.* (2022) 100116.
- [62] P. Politzer, K.C. Daiker, Models for chemical reactivity. In: Deb BM, editor. *The Force Concept in Chemistry*. New York: Van Nostrand Reinhold. (1981). 294-387.
- [63] A. Ram Kumar, S. Selvaraj, M. Azam, G.P. Sheeja Mol, N. Kanagathara, M. Alam, P. Jayaprakash, Spectroscopic, Biological, and Topological Insights on Lemonol as a Potential Anticancer Agent. *ACS omega*, 8 (2023) 31548-31566, <https://doi.org/10.1021/acsomega.3c04922>.
- [604] S. Selvaraj, A. Ram Kumar, T. Ahilan, M. Kesavan, G. Serdaroglu, P. Rajkumar, M. Mani, S. Gunasekaran, and S. Kumaresan, Experimental and Theoretical Spectroscopic Studies of the Electronic Structure of 2-Ethyl-2-phenylmalonamide, *Phys. Chem. Res.* 10 (2022) 333-344, <https://doi.org/10.22036/PCR.2021.304087.1966>.
- [65] A. Ram Kumar, S. Selvaraj, K.S. Jayaprakash, S. Gunasekaran, S. Kumaresan, J. Devanathan, K.A. Selvam, L. Ramadass, M. Mani, P. Rajkumar, Multi-spectroscopic (FT-IR, FT-Raman, ¹H NMR and ¹³C NMR) investigations on syringaldehyde, *J. Mol. Struct.* 1229 (2021) 129490, <https://doi.org/10.1016/j.molstruc.2020.129490>.
- [66] S. Selvaraj, A. Ram Kumar, T. Ahilan, M. Kesavan, S. Gunasekaran, and S. Kumaresan, Multi spectroscopic and computational investigations on the electronic structure of oxyclozanide, *J. Indian. Chem. Soc.* 99 (2022) 10-0-676, <https://doi.org/10.1016/j.jics.2022.100676>.
- [67] R. Mohamed Asath, R. Premkumar, T. Mathavan, A. Milton Franklin Benial, Structural, spectroscopic and molecular docking studies on 2-amino-3-chloro-5-trifluoromethyl pyridine: A potential bioactive agent, *Spectrochim. Acta - Part A Mol. Biomol. Spectrosc.* 175 (2017) 51–60. <https://doi.org/10.1016/j.saa.2016.11.037>.
- [68] H. Louis, L. Guo, S. Zhu, S. Hussain, T. He, Computational study on interactions between CO₂ and (TiO₂)_n clusters at specific sites, *Chin. J. Chem. Phys.* 32 (6) (2019) 674–686. <https://doi.org/10.1063/1674-0068/cjcp1905108>

- [69] A. Udoikono, H. Louis, E. Eno, E.C. Agwamba, T.O. Unimuke, A.T. Igbalagh, A.S. Adey, Reactive azo compounds as a potential chemotherapy drugs in the treatment of malignant glioblastoma (GBM): Experimental and theoretical studies, *J. Photochem. Photobiol. A.* (2022) 100116. <https://doi.org/10.1016/j.jpap.2022.100116>
- [70] P. Politzer, K.C. Daiker, Models for chemical reactivity. In: Deb BM, editor. *The Force Concept in Chemistry*. New York: Van Nostrand Reinhold. (1981). 294-387.
- [71] K. Boudebbous, H. Boulebd, C. Derabli, L. Bendjeddou, C. Bensouici, D. Harakat, H. Merazig, A. Debache. Synthesis, crystal structure, Hirshfeld surface, biological evaluation, docking study, DFT calculations, and *in silico* ADME analysis of naphto-1,3-oxazin-3(2*H*)-one derivatives as dual promising Inhibitors of Cholinesterase and α -Glucosidase. *Journal of Molecular Structure*, 1225 (2021) 129103. <https://doi.org/10.1016/j.molstruc.2020.129103>.
- [72] K. Boudebbous, H. Boulebd, C. Bensouici, D. Harakat, R. Boulcina, A. Debache. Synthesis, docking study and biological activities evaluation of 1-amidoalkyl-2-naphthol derivatives as dual inhibitors of cholinesterase and α -glucosidase. *ChemistrySelect*, 5 (2020) 3515-3520. <https://doi.org/10.1002/slct.202000558>.
- [73] A. Ram Kumar, S. Selvaraj, N. Kanagathara, Spectroscopic, Structural and Molecular Docking Studies on N, N-Dimethyl-2-[6-methyl-2-(4-methylphenyl) Imidazo [1, 2-a] pyridin-3-yl] Acetamide, *Phys. Chem. Res.*12(1) (2024) 95-107, <https://doi.org/10.22036/PCR.2023.387911.2306>.
- [74] P. Politzer, P.R. Laurence, K. Jayasuriya, Molecular electrostatic potentials: An effective tool for the elucidation of biochemical phenomena, *Environ. Health Perspect.*, 61 (1985) 191–202. <https://doi.org/10.1289/ehp.8561191>.
- [75] P. Politzer, J.S.Murray, *Theoretical Biochemistry and Molecular Biophysics: A Comprehensive Survey*. Vol. 2. Schenectady, NY: Adenine Press. (1991). 165-191
- [76] P. R. Spackman *et al.*, “CrystalExplorer: A program for Hirshfeld surface analysis, visualization and quantitative analysis of molecular crystals, *J. Appl. Crystallogr.*, 4, (2021) 1006–1011. <https://doi.org/10.1107/S1600576721002910>.
- [77] M. A. Spackman, D. Jayatilaka, Hirshfeld surface analysis, *Cryst. Eng. Comm.*, 11, (2009), 19–32, <https://doi.org/10.1039/b818330a>.
- [78] M. A. Spackman, J. J. McKinnon, and D. Jayatilaka, “Electrostatic potentials mapped on Hirshfeld surfaces provide direct insight into intermolecular interactions in crystals, *Cryst. Eng. Comm.*, 10 (2008) 377–388. <https://doi.org/10.1039/b715227b>.
- [79] M. A. Spackman and J. J. McKinnon, “Fingerprinting intermolecular interactions in molecular crystals, *Cryst. Eng. Comm.*, 4 (2008) 2378–392 doi: 10.1039/b203191b.
- [80] C. F. Mackenzie, P. R. Spackman, D. Jayatilaka, and M. A. Spackman, “CrystalExplorer model energies and energy frameworks: Extension to metal coordination compounds, organic salts, solvates and open-shell systems,” *IUCr J.*, 4, (2017) 575–587. <https://doi.org/10.1107/S205225251700848X>.
- [81] M. J. Turner, S. P. Thomas, M. W. Shi, D. Jayatilaka, M. A. Spackman, “Energy frameworks: Insights into interaction anisotropy and the mechanical properties of

molecular crystals, Chem. Comm., 51 (2015) 3735-3738, <https://doi.org/10.1039/c4cc09074h>.

Graphical abstract

An efficient protocol for the synthesis of the pyrano[4,3-b]pyran derivatives via a three component reaction was developed. The work was completed by the confirmation of one compound by X-ray diffraction and its Hirshfeld surface analyzed. The biological evaluation, DFT calculations and molecular docking were also carried out.



Credit author statement

Yasmine Zine: Investigation, Writing. **Mohamed Abdsselem Dems:** Investigation, Writing.
Raouf Boulcina: Writing - Review. **Ali Boudjada:** Investigation, Writing **Dominique Harakat:**
Investigation. **Thierry Roisnel;** Investigation, **Anthony Robert:** Investigation.
Abdelmadjid Debache: Writing, Review, Supervision, Project administration, Validation.

Declaration of interests

The authors declare that they have no known competing financial interests or personal relationships that could have appeared to influence the work reported in this paper.

The authors declare the following financial interests/personal relationships which may be considered as potential competing interests: